A Coupling Approach between Resolved and Coarse-grid Sub-channel CFD

B. Liu [a,*], S. He [a], C. Moulinec [b] and J. Uribe [c]
[a] Department of Mechanical Engineering, University of Sheffield, Sheffield, S3 7QB, UK
[b] Science and Technology Facilities Council, Daresbury Laboratory, Warrington, WA4 4AD, UK
[c] EDF Energy R&D UK Centre, Manchester, M13 9PL, UK
[*] Correspondence: bo.liu@sheffield.ac.uk

Abstract

As a follow-up development of the Computational Fluid Dynamics (CFD)-based sub-channel analysis tool, i.e. coarse-grid Sub-Channel CFD (SubChCFD), this paper aims at developing a coupling between SubChCFD and resolved CFD, thereby enhancing the performance and application flexibility of the coarse-grid model. A time-explicit domain-overlapping method is used to achieve the coupling, which ensures good flexibility and reasonable numerical stability. In such a coupling framework, embedded resolved sub-models are to be placed arbitrarily into a SubChCFD baseline model in regions selected for refinement. Two coupling modes are available: the one-way coupling mode, where the SubChCFD model provides the boundary conditions for the resolved sub-models, but no feedback from the resolved sub-model to the SubChCFD model is carried out; the two-way coupling mode, where feedback is enabled from the resolved sub-model back to the SubChCFD model to improve the solution of the latter.

The coupling methodology has been first tested using 2-D flow cases, including an internal flow in a T-junction and an external flow passing a square cylinder. It has then been applied to 3-D cases of nuclear rod bundles with complex conditions. One is a 7×7 rod bundle with locally 'ballooned' fuel rods where complex flow phenomena occur due to the blockage effect caused by area reduction in flow passages. The other is a 5×5 rod bundle with inward jet flow at one corner of the housing walls resulting in a strong cross flow. In all of the test cases, the results of the coarse-grid SubChCFD model with the two-way coupling approach are consistently improved compared with those of the uncoupled SubChCFD simulations.

Keywords

CFD, Coarse-grid, Coupling, Domain overlapping, Nuclear rod bundle, Sub-channel

1. Introduction

With the recent development in the nuclear industry, reactor design and safety assessment have put forward increasingly challenging requirements for thermal hydraulic analysis. The traditional 0-D/1-D tools, restricted by their model architecture, become increasingly inadequate to meet these requirements, especially in handling situations with significant 3-D phenomena and flow transients (Brockmeyer et al., 2016; Papukchiev et al., 2009). The advanced Computational Fluid Dynamics (CFD) method is in principle superior to the traditional tools, but it still suffers from a long turnaround in computation time, which limits its application in addressing realistic engineering problems (Hanna et al., 2020; Viellieber and Class, 2015). To fill the gap, a hybrid technique, a CFD-based sub-channel analysis tool, has been proposed in our previous work (Liu et al., 2019), which is referred to as Sub-Channel CFD (SubChCFD).

SubChCFD is a mix of CFD and sub-channel codes, taking advantage of both. Thanks to its CFD-like architecture, SubChCFD is capable of providing higher resolution results than the latter, therefore allows more detailed physics to be captured. Meanwhile, the computing cost is much lower than conventional CFD due to the use of a very coarse mesh system, which potentially enables routine numerical simulations to be carried out for large reactor components or even the entire reactor core. Similar to sub-channel codes, fully validated industry-standard correlations are employed for wall modelling closure to ensure a higher modelling consistency so as to reduce the uncertainty of numerical simulations for specific designs of reactors. A detailed description of the baseline SubChCFD can be found in Liu et al. (2019).

As it is based on a more general and advanced CFD platform, SubChCFD is, in principle, more flexible and better suited than typical sub-channel codes in describing complex flow and heat transfer behaviours of coolant in reactors at off-design conditions. However, the conditions should not deviate too much from the ‘standard’ ones, as the experimental data or correlations used for the model closure may become invalid and, therefore, result in significant uncertainties. For example, a local blockage caused by fuel rod ballooning during a Loss of Coolant Accident (LOCA) of a Pressurised Water-cooled Reactor (PWR) (Ang et al., 1988) would be a challenge for SubChCFD, since the typical sub-channel structure is significantly distorted around the blockage because of the deformation of the fuel rods, making the empirical correlations no longer valid for these structures.

A solution to handle such situations is to take advantage of one of the main strengths of SubChCFD, i.e. its readiness to be coupled with other CFD based methods. Through coupling with conventional CFD (referred to as ‘resolved CFD’ throughout this paper), the empiricism-based closure method in

SubChCFD can be locally 'overridden' or 'replaced' by nesting resolved sub-models in selected regions where the flow exhibits complex features. Work to be presented in this paper is aimed at developing such a coupling functionality to enhance the performance of SubChCFD so that it can be used for a wider range of scenarios especially those with complex local flow features.

The concept of coupling different simulation packages/methodologies has been widely used in nuclear applications, an important example of which is the coupling between 1-D system/sub-channel codes and CFD (Aumiller et al., 2001; Bandini et al., 2015; Bavière et al., 2014; Bertolotto et al., 2009; Bury, 2013; Gibeling and Mahaffy, 2002; Grunloh and Manera, 2017, 2016, Papukchiev et al., 2009, 2015, 2011; Pialla et al., 2015; Toti et al., 2017). In such approaches, the 1-D code, which has normally been validated against numerous engineering data and experiences, provides reasonable boundary conditions for the CFD models so that they can be used more efficiently to account for some key components/parts with complex 3-D phenomena and/or flow transients that cannot be well represented by the 1-D approaches. This enables the CFD methods to play some role in reactor system modelling, alleviating, to some extent, the difficulties arising from their high computing costs.

In general, there are two approaches for the aforementioned coupling described in the literature on the basis of the treatment of the computational domain, including domain decomposition (Aumiller et al., 2001; Bertolotto et al., 2009; Gibeling and Mahaffy, 2002; Papukchiev et al., 2009; Toti et al., 2017) and domain overlapping (Bavière et al., 2014; Grunloh and Manera, 2017, 2016) methods. Detailed comparisons are also made between the two approaches (Bandini et al., 2015; Papukchiev et al., 2015). Earlier coupling efforts for nuclear applications reported in the open literature are mostly based on the domain decomposition approach as it is more intuitive and easy to implement (Aumiller et al., 2001; Gibeling and Mahaffy, 2002). In such an approach, the entire computational domain is decomposed into several sub-domains, some of which are simulated using CFD, and the rest are accounted for using system/sub-channel code. Coupling is achieved by dynamically exchanging data at the interfaces between the CFD and the system/sub-channel code domains to obtain the necessary boundary conditions. To ensure convergence and numerical stability, the domain decomposition method normally requires the solutions of the coupled sub-models to be close to each other at the coupling interfaces during the simulation. This often leads to the use of very small time steps in an explicit approach or high under-relaxation in a semi-implicit approach. In the domain overlapping method however, a base mesh that covers the entire computational domain is always created for system/sub-channel code, whereas CFD is used for some selected regions. This keeps the mathematical system of the system/sub-channel code model intact and consistent with the CFD system, thus improving numerical stability (Grunloh and Manera, 2016). In the overlapping region, the CFD solution is used as feedback to correct the solution of the system/sub-channel code, which therefore improves the overall performance of the simulation.

Despite the similarities with the aforementioned domain overlapping approaches, the coupling to be developed in this paper is very different in terms of its technical implementation, such as the 3-D-to-3-D data exchange algorithm at the coupling interfaces, and the forms of information feedback between sub-models. In this respect, its principle is very close to the concept of the overset mesh method (Clark et al., 2014; Jarkowski1 et al., 2014; Norman et al., 2002; Sitaraman et al., 2008; Vassberg et al., 2002; Wissink et al., 2008). The strategy of the overset mesh method is to decompose complex geometry into a number of sub-regions each of which can be represented using simpler meshes (Norman et al., 2002). Domain connectivity algorithms are usually employed to bridge these meshes through interpolative data exchanges. This method allows multiple layers of different types of meshes and the corresponding CFD solvers to be used in a single CFD simulation. For example, a curvilinear structured or prismatic unstructured grid can be used in the near-wall regions to properly capture the geometry and the boundary layer, whereas a structured Cartesian grid can be used for the regions at some distance away from the wall, on which high order numerical schemes are easier to be implemented.

In practice, special numerical tools are developed to locate the 'donor' and the 'acceptor' grid points through which data are exchanged in the form of Dirichlet boundaries (Sitaraman et al., 2008). At each time step, iterations are performed over the sub-meshes until convergence is achieved before advancing to the next time step. In some of the later versions of the overset mesh method, the creation, positioning and refinement of the sub-meshes as well as the 'hole cutting' process (removal of the grid points of the background coarse mesh in the overlapping region) are performed automatically, which relies on two directions of data transfer (Kim et al., 2005). The first one is referred to as the 'upward marching', which starts from the coarsest background mesh, identifying the regions for which the foreground finer meshes are created based on the solution error of the initial results on the background mesh. The second one is the so-called 'downward marching', through which information is passed back from the finer meshes to the coarser ones to update the boundary conditions of the latter at the fringe grid points in the overlapping regions so that the accuracy of the results on those meshes can be improved as a result. From the perspective of spatial arrangement of the sub-domains, the overset mesh method is more likely to be a domain decomposition approach, as the grid points of the coarse meshes located within the overlapping region are normally 'blanked out' from the solution domain and the result improvements rely purely on boundary condition update at a number of 'artificially' created 'internal' boundaries. The disadvantage of such a treatment is that it may cause inconsistency at these boundaries for the different meshes and hence numerical instability. Despite this, the 3-D data exchange methods at the coupling interfaces used in the overset mesh method are still of much use and can be borrowed for the current development.

In the current development, domains for the SubChCFD and resolved CFD are determined pre-simulation and no dynamic adaptation is needed. In addition, the grid points of the SubChCFD mesh located within the overlapping region are not removed from the solution domain, thus ensuring the intactness of SubChCFD's mathematical system. However, the embedded resolved sub-models naturally need to receive data from the SubChCFD results to define and update their boundary conditions. Simulation results of the SubChCFD model can also be improved through feedbacks of the resolved sub-models in the form of additional source terms, which is similar to the domain overlapping coupling method between system/sub-channel codes and CFD. In this way, the improved SubChCFD results can in turn provide more accurate boundary conditions for the embedded resolved sub-model, and thereby improve the overall accuracy of the coupling system.

In Section 2 of this paper, the technical details of the methodology are described. In Section 3, simple flow cases are used first to verify the effectiveness of the coupling platform developed, and then the coupling technique is applied to practical nuclear fuel bundle cases for further testing and validation. Conclusions are given in Section 4 and directions for future work are also indicated.

2. Methodology

2.1 A brief introduction to SubChCFD

As explained in the introduction, SubChCFD is a blend of CFD and sub-channel code methodology (Liu et al., 2019). A dual mesh approach is used, including, namely, (i) a filtering mesh which aligns with the mesh used in typical sub-channel codes, enabling the integral wall friction and heat transfer effects calculated using existing engineering correlations, and (ii) a computing mesh, on which the Reynolds Average Navier-Stokes (RANS) equations are solved with a near wall closure method based on calculations of step (i). Figure 1 shows an example of the dual mesh system for a PWR fuel channel, in which the computing mesh is created by sub-dividing a filtering mesh cell.

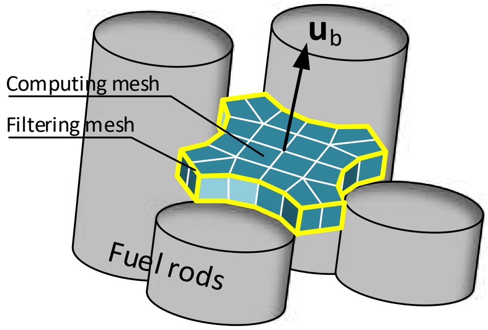

Fig. 1 Mesh system in SubChCFD

The Finite Volume (FV) RANS momentum equation written for a collocated arrangement of the unknowns to be solved in SubChCFD can be written as follows,

$$\frac{\Omega}{\Delta t}\left(\rho^{n+1}\vec{\boldsymbol{u}}^{n+1}-\rho^{n}\vec{\boldsymbol{u}}^{n}\right)+\oint_{S}\vec{\boldsymbol{u}}^{n+1}\left(\vec{\boldsymbol{J}}^{n}\cdot\vec{\boldsymbol{n}}\right)dS=-\oint_{S}\left(\bar{\bar{I}}p\cdot\vec{\boldsymbol{n}}\right)dS+\oint_{S}\left(\bar{\bar{\sigma}}^{n+1}\cdot\vec{\boldsymbol{n}}\right)dS+\Omega\vec{\boldsymbol{S}}_{M}^{n} \qquad (1)$$

where Ω is the cell volume, Δt is the time step size, ρ is fluid density, superscript n and n+1 represent the n$^{\text{th}}$ and the (n+1)$^{\text{th}}$ time step, respectively, $\vec{\boldsymbol{u}}$ is the velocity vector, $\vec{\boldsymbol{J}}$ is the convective mass flux, $\vec{\boldsymbol{n}}$ is the unit normal vector to the cell surface, S is the area of the cell surface, $\bar{\bar{I}}$ is the unit tensor, $\bar{\bar{\sigma}}$ is the stress tensor including both the viscous and turbulence contributions, $\vec{\boldsymbol{S}}_M$ is the body force. In SubChCFD, each term of the above equation is treated no differently from a standard FV approach except for the (molecular and turbulent) diffusion term which may be the main error source when using a very coarse mesh to simulate wall bounded shear flows. In SubChCFD, it is decomposed into an interior part and a wall boundary part as follows,

$$\oint_{S}\bar{\bar{\sigma}}\cdot\vec{\boldsymbol{n}}dS=\int_{S_w}\bar{\bar{\sigma}}\cdot\vec{\boldsymbol{n}}dS+\int_{S_f}\bar{\bar{\sigma}}\cdot\vec{\boldsymbol{n}}dS \qquad (2)$$

where S_w is the cell surfaces adjacent to a wall boundary, S_f is the interior cell surfaces. The interior part in Equation 2 is further written as

$$\int_{S_f}\bar{\bar{\sigma}}\cdot\vec{\boldsymbol{n}}dS=\int_{S_f}\left(\mu+\mu_t\right)\left[\nabla\vec{\boldsymbol{u}}+\left(\nabla\vec{\boldsymbol{u}}\right)^{\mathrm{T}}-\frac{2}{3}\delta\nabla\cdot\vec{\boldsymbol{u}}\right]\cdot\vec{\boldsymbol{n}}dS\,, \qquad (3)$$

and the eddy viscosity μ_t is modelled using appropriate turbulence models. Since the computing mesh is very coarse, it is reasonable to assume that Equation 3 is always applied in the core of the flow where turbulence is strong. In the initial version of SubChCFD, a mixing length model was used and proved to be sufficient to predict a correct level of turbulence for the flow away from the wall (Liu et al., 2019). In this paper, the mathematical system of SubChCFD is slightly updated to be compatible with some more advanced 2-equation turbulence models (e.g. k-ε and k-ω series of turbulence models). However, using such turbulence models in SubChCFD is not aimed at improving the prediction of the near-wall turbulence and producing more accurate results of the wall shear stresses. Instead, the main purpose is to simplify the information exchange of turbulence quantities with the coupled resolved fine-mesh models where more advanced RANS turbulence models are usually used.

The wall boundary part, however, is calculated making use of sub-channel friction correlations to ensure a correct integral effect of the wall friction:

$$\int_{S_w} \bar{\bar{\sigma}} \cdot \vec{\boldsymbol{n}} dS = -\frac{1}{4} f \frac{1}{2} \rho_b \vec{\boldsymbol{u}}_{\boldsymbol{b}} \left|\vec{\boldsymbol{u}}_{\boldsymbol{b}}\right| \int_{S_w} dS \tag{4}$$

where f denotes the skin friction factor, ρ_b and $\vec{\boldsymbol{u}}_{\boldsymbol{b}}$ represent the sub-channel bulk density and bulk velocity derived by averaging the CFD solutions over the corresponding sub-channels. A correlation is given as follows to calculate the friction factor along a square-lattice rod bundle (Todreas and Kazimi, 1990),

$$f = \left[a + b_1 \left(\frac{P}{D_h} - 1 \right) + b_2 \left(\frac{P}{D_h} - 1 \right)^2 \right] / \mathrm{Re}^n \tag{5}$$

where the values of the parameters for different types of sub-channels are given in Table 1.

Table 1 Parameters in the friction factor correlation for square-lattice rod bundles

Sub-channel type	a	b_1	b_2	n
Interior (laminar)	35.55	263.7	-190.2	1
Edge (laminar)	44.40	256.7	-267.6	1
Corner (laminar)	58.83	160.7	-203.5	1
Interior (turbulent)	0.1339	0.09059	-0.09926	0.18
Edge (turbulent)	0.143	0.04199	-0.04428	0.18
Corner (turbulent)	0.1452	0.02681	-0.03411	0.18

2.2 Fundamentals of the coupling methodology

SubChCFD is, in essence, a sub-channel analysis tool implemented on CFD platform. Consequently, some of the concepts described in the introduction can be used to facilitate its coupling with resolved CFD. Obviously, the domain overlapping method has advantages in the current application, as it not only maintains the independence of the coupled sub-models, leading to higher numerical robustness, but also simplifies the mesh system generation by a large extent.

To achieve the coupling between SubChCFD and resolved CFD models, a time-explicit domain overlapping method is used, which provides good flexibility and reasonable numerical stability. From a temporal point of view, information exchange between the coupled models only happens at the end of each time step (Sub-iteration within time step is also allowed in the current coupling scheme, which is helpful for deriving time-accurate results in simulations of strong transient problems. In that case, the information exchange happens at the end of each sub-iteration.), resulting in a relatively 'loose' coupling and ensures, to some extent, high independence of the coupled models. From a spatial point of view, the domain overlapping method strengthens such an independence and, more importantly, avoids potential numerical issues caused by the interfacial mesh non-conformality (which may happen in a domain decomposition approach). In addition, the domain overlapping greatly simplifies mesh generation. For example, it is not necessary to ensure that the grid lines of the coupled sub-meshes coincide with each other. This therefore provides the user high flexibility to embed one or more resolved sub-domains arbitrarily into selected regions of an existing coarse-grid domain to achieve result refinement over these regions. Figure 2 shows a sketch of the mesh arrangement used in the current coupling method.

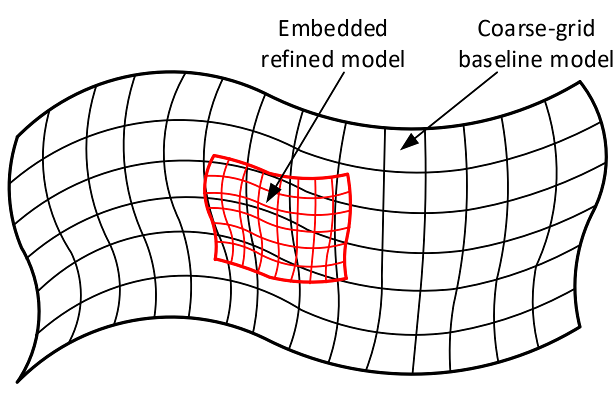

Fig. 2 Sketch of mesh arrangement in the domain-overlapping coupling

As described above, the coarse-grid model is applied to cover the entire domain and can be solved independently without relying on the embedded resolved sub-models. In contrast, the embedded sub-model needs information from the coarse-grid model to define its boundary conditions. Feedback from the resolved sub-model to the coarse-grid model is also allowed for overall accuracy improvement, which leads to a two-way coupling (detailed theory about this is elaborated on in Section 2.3). It is the user's choice whether to allow a two-way coupling or not. Figure 3 illustrates the data flow in this coupling system.

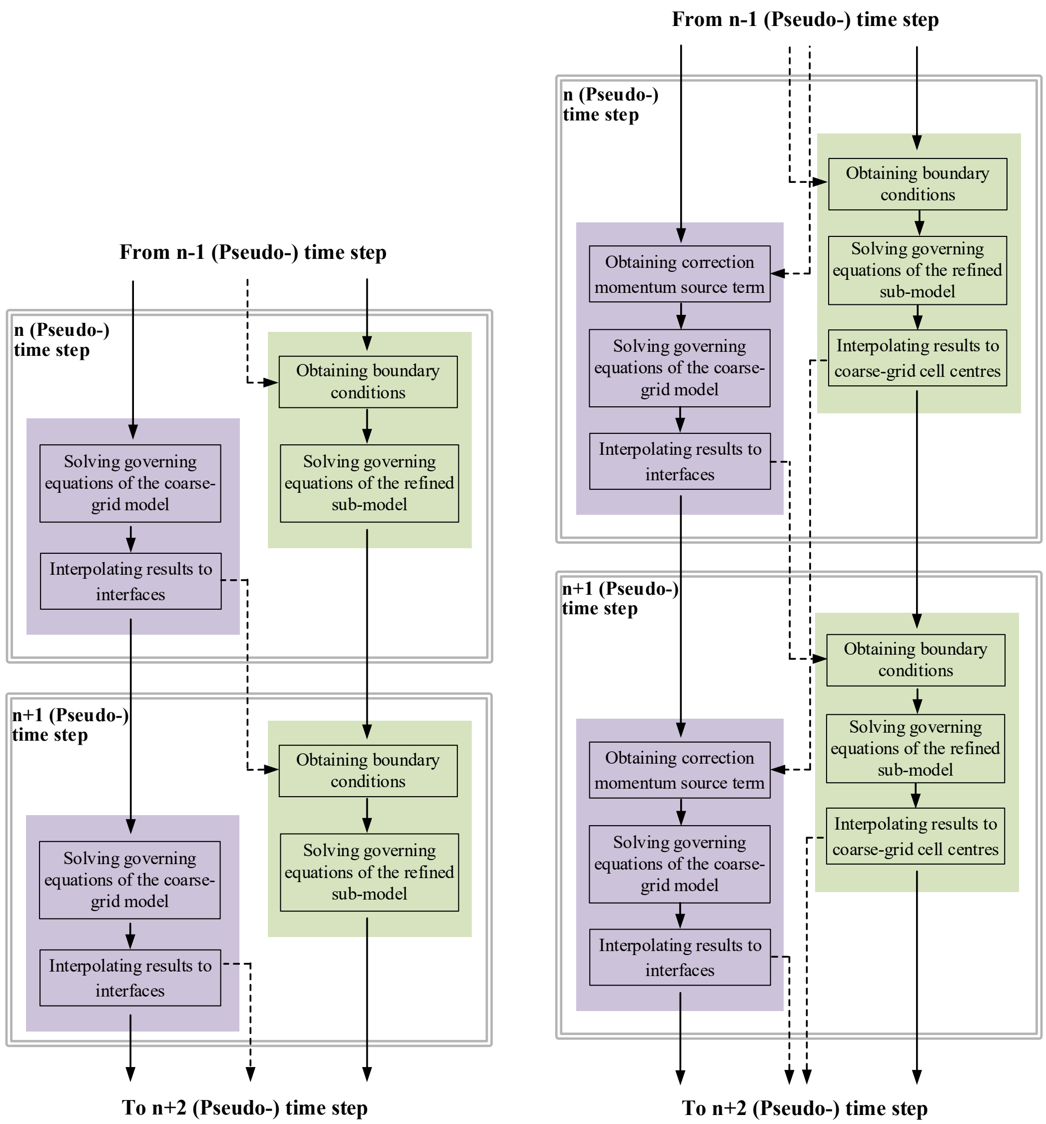

(a) (b)

Fig. 3 Data flow in the coupling system: (a) one-way coupling, (b) two-way coupling

The method has been implemented in a pressure-based FV CFD solver Code_Saturne (Fournier et al., 2011). A Dirichlet velocity boundary condition (i.e. specification of boundary values) is used for the momentum equation and a homogeneous Neumann condition (i.e. zero normal gradient) is used correspondingly for the Poisson equation of the pressure correction at the boundaries formed by the coupling interfaces in the embedded sub-domain. The pressure of the fine mesh at a chosen reference point was fixed to that of the coarse-mesh solution. Other physical boundaries (e.g. solid walls) are treated no differently from a standard RANS approach. For simplicity, an example is given in Figure 4, showing how the Dirichlet interface velocity is calculated in the case of a coupled 2-D triangular mesh system. The calculation method can be straightforwardly extended to arbitrary types of 3-D meshes.

To increase the numerical stability of the coupled simulation, both the fine-mesh and the coarse-mesh velocities of the previous time step are used to obtain the velocity boundary condition for the embedded sub-model. As can be seen in Figure 4, the interface velocity at target face centre F in the fine mesh is calculated using the velocities at cell centre I (the cell adjacent to face F in the fine mesh) and J (the cell closest to I in the coarse mesh), respectively. By making use of the respective velocity gradient at these cell centres, the two velocities are projected onto the orthogonal line I'J' to face F at locations with equal distance to point F. Then, the interface velocity $\vec{\boldsymbol{u}}_F$ is calculated as an equal-weighted blending of them using the following equation,

$$\vec{\boldsymbol{u}}_F = 0.5\left[\vec{\boldsymbol{u}}_J + \nabla\vec{\boldsymbol{u}}_J \cdot \left(\overrightarrow{JJ'} + \overrightarrow{O'F}\right)\right] + 0.5\left[\vec{\boldsymbol{u}}_I + \nabla\vec{\boldsymbol{u}}_I \cdot \left(\overrightarrow{II'} + \overrightarrow{O'F}\right)\right]. \quad (6)$$

Similar calculations are applied to all other scalars to be solved, such as turbulence quantities in a turbulent flow or thermal variables in a non-isothermal flow.

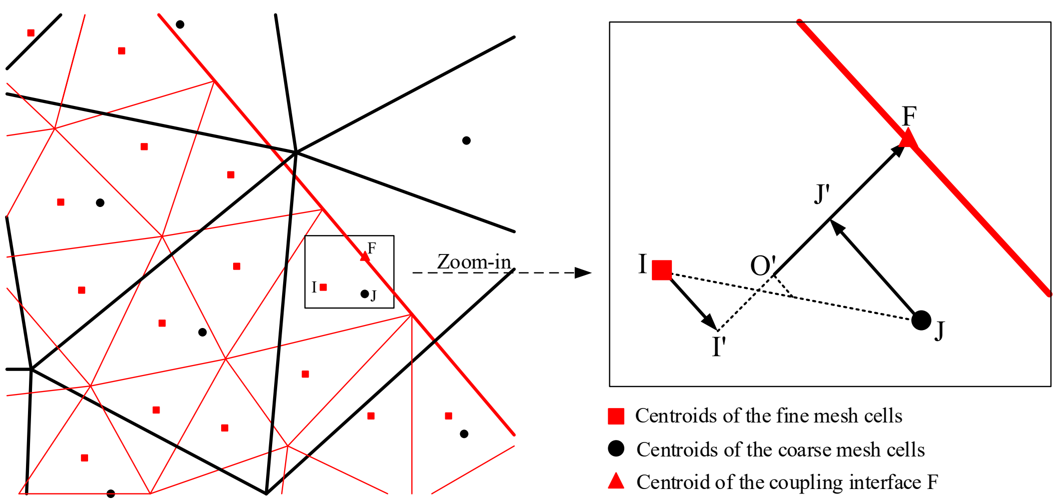

Fig. 4 Calculation of the interface velocity

It is worth pointing out that, to ensure the numerical algorithm to solve the governing equations of the embedded sub-model well-posed, the Dirichlet velocity boundary conditions defined should satisfy the global mass conservation a priori (Tang et al., 2003). This is approximately guaranteed in the coupling, as the boundaries of the embedded sub-domain, consisting of the physical boundaries and the coupling interfaces, form a close surface within the coarse-grid domain and the velocities at the coupling interfaces (calculated using Equation 6) are based on the velocity solution that satisfies the conservation of mass everywhere at the coarse-mesh level. Despite this, there may still be a minor global mass imbalance at the fine-mesh level due to interpolation and the magnitude of such an imbalance depends on the interpolation scheme used and the difference in mesh resolution between the coupled model pair. In order to achieve a strict mass balanced boundary of the embedded sub-domain, a weighted flux correction approach (Völkner et al., 2017) is introduced to correct the velocities at the coupling interfaces before they are used as Dirichlet boundary conditions.

As mentioned above, a two-way coupling can be enabled by allowing feedback from the embedded sub-models to the coarse-grid model. This is aimed at improving the local accuracy of the coarse-mesh solution. In fact, the improvement will not be limited to just the overlapping region but will propagate beyond due to transport effect of the flow. The improved coarse-mesh solution, in turn, allows for a more accurate definition of the Dirichlet boundaries for the embedded sub-model. Therefore, the overall accuracy of the whole coupling is improved.

In the current implementation, a correction source term is used to achieve such a feedback, i.e. by adding a source term to the FV discrete momentum equation (Equation 1) of the coarse-grid baseline model as a penalty to force the velocity of this model to approach that of the refined sub-model. The equation to be solved in the coarse-grid model then reads as

$$\frac{\Omega}{\Delta t}\left(\rho^{n+1}\vec{\boldsymbol{u}}^{n+1}-\rho^{n}\vec{\boldsymbol{u}}^{n}\right)+\oint_{S}\vec{\boldsymbol{u}}^{n+1}\left(\vec{\boldsymbol{J}}^{n}\cdot\vec{\boldsymbol{n}}\right)dS=-\oint_{S}\left(\overline{\overline{I}}p\cdot\vec{\boldsymbol{n}}\right)dS+\oint_{S}\left(\overline{\overline{\sigma}}^{n+1}\cdot\vec{\boldsymbol{n}}\right)dS+\Omega\vec{\boldsymbol{S}}_{M}^{n}+\Omega\vec{\boldsymbol{S}}_{\Delta}^{n} \qquad (7)$$

where $\vec{\boldsymbol{S}}_{\Delta}^{n}$ denotes the correction source term which is based on the local velocity difference between the two coupled models, taking the following form:

$$\vec{\boldsymbol{S}}_{\Delta}^{n}=\lambda\frac{\rho^{n}}{\Delta t}(\vec{\boldsymbol{u}}_{dis}^{n}-\vec{\boldsymbol{u}}_{loc}^{n})\,. \qquad (8)$$

In the above equation, $\vec{\boldsymbol{u}}_{loc}^{n}$ is the cell centre velocity of the local coarse-grid model, $\vec{\boldsymbol{u}}_{dis}^{n}$ is the velocity of the distant embedded sub-model interpolated from the closest cell centre to the location where $\vec{\boldsymbol{u}}_{loc}^{n}$ is stored, λ is a user prescribed correction factor, representing to what extent the coarse-mesh result is expected to be corrected by that of the resolved model. A too high value of λ may cause strong oscillations in the simulation. The authors suggest $\lambda < 1.0$ for a steady flow and $\lambda < 0.1$ for a strongly transient flow.

2.3 Pressure reconstruction in the two-way coupling

As depicted in Section 2.2, a correction momentum source term is used in the two-way coupling to increase the overall accuracy of the coarse-grid model. Ideally, the correction source term should not play a role except offsetting the truncation error that arises due to the use of a coarse mesh. Before giving a more detailed analysis on this, the differential form of the RANS governing equations is recalled:

$$\frac{\partial \rho}{\partial t} + \nabla \cdot (\rho \vec{\boldsymbol{u}}) = 0 \tag{9}$$

$$\frac{\partial (\rho \vec{\boldsymbol{u}})}{\partial t} + \nabla \cdot (\rho \vec{\boldsymbol{u}} \otimes \vec{\boldsymbol{u}}) = -\nabla p + \nabla \cdot \bar{\bar{\sigma}} + \vec{\boldsymbol{S}}_M , \tag{10}$$

For ease of analysis, let $\psi(\rho, \vec{\boldsymbol{u}}) = \nabla \cdot (\rho \vec{\boldsymbol{u}} \otimes \vec{\boldsymbol{u}}) - \nabla \cdot \bar{\bar{\sigma}} - \vec{\boldsymbol{S}}_M$, the momentum equation, i.e. Equation 10, can be written in the following form:

$$\frac{\partial (\rho \vec{\boldsymbol{u}})}{\partial t} + \psi(\rho, \vec{\boldsymbol{u}}) = -\nabla p \, . \tag{11}$$

Accordingly, the spatial discrete form of Equation 11 on a coarse mesh and a fine mesh can be given by the following equations, respectively,

$$\frac{\partial (\rho_c \vec{\boldsymbol{u}}_c)}{\partial t} + \hat{\psi}^c(\rho_c, \vec{\boldsymbol{u}}_c) = -\hat{\nabla}^c(p_c) \tag{12}$$

$$\frac{\partial (\rho_f \vec{\boldsymbol{u}}_f)}{\partial t} + \hat{\psi}^f(\rho_f, \vec{\boldsymbol{u}}_f) = -\hat{\nabla}^f(p_f) , \tag{13}$$

where the variables with subscripts c and f denote those associated with the coarse mesh and the fine mesh, respectively. $\hat{\psi}^c$ and $\hat{\psi}^f$ represent a certain discrete form of operator ψ on the coarse mesh and the fine mesh and $\hat{\nabla}^c$ and $\hat{\nabla}^f$ are the respective discrete gradient operators.

The momentum equation solved for the coarse-grid model in the two-way coupling can be written as follows:

$$\frac{\partial (\rho_{cpl} \vec{\boldsymbol{u}}_{cpl})}{\partial t} + \hat{\psi}^c(\rho_{cpl}, \vec{\boldsymbol{u}}_{cpl}) = -\hat{\nabla}^c(p_{cpl}) + \vec{\boldsymbol{S}}_\Delta , \tag{14}$$

where $\vec{\boldsymbol{u}}_{cpl}$ is the numerical solution of velocity in the coupled simulation, the error norm of which is expected to satisfy the following relation:

$$\left\|\vec{\boldsymbol{u}}_c - \vec{\boldsymbol{u}}\right\| > \left\|\vec{\boldsymbol{u}}_{cpl} - \vec{\boldsymbol{u}}\right\| > \left\|\vec{\boldsymbol{u}}_f - \vec{\boldsymbol{u}}\right\|. \tag{15}$$

As such, solving Equation 14 is, to some extent, equivalent to solving an equation with the spatial discretisation error of operator ψ in between those of Equations 12 and 13, which may be written in the following form:

$$\frac{\partial(\rho_{cpl}\vec{\boldsymbol{u}}_{cpl})}{\partial t} + \tilde{\psi}^c(\rho_{cpl}, \vec{\boldsymbol{u}}_{cpl}) = -\hat{\nabla}^c(\phi_{cpl}), \tag{16}$$

where $\tilde{\psi}$ is some unknown discrete form of the operator ψ. The exact form of it is unknown, but the purpose is to obtain a more accurate solution than that of Equation 12, although the same coarse mesh is used. In addition, it should be noted that ϕ_{cpl} in Equation 16 is not equal to p_{cpl} in Equation 14, which is a unique problem to address in the two-way coupling of this paper. Unfortunately, ϕ_{cpl} is the real physical pressure field to be obtained rather than the pressure solution of Equation 14, i.e. p_{cpl}. This is why a pressure reconstruction process is required.

To obtain ϕ_{cpl}, the correction source term $\vec{\boldsymbol{S}}_\Delta$ is decomposed into an effective part $\vec{\boldsymbol{S}}'$ and a potential field $\vec{\boldsymbol{S}}''$ as follows,

$$\vec{\boldsymbol{S}}_\Delta = \vec{\boldsymbol{S}}' + \vec{\boldsymbol{S}}'', \tag{17}$$

where $\vec{\boldsymbol{S}}''$ is the gradient of a scalar field χ and can be written as

$$\vec{\boldsymbol{S}}'' = \hat{\nabla}^c(\chi). \tag{18}$$

The potential component $\vec{\boldsymbol{S}}''$ does not cause any changes to the velocity solution but only acts a correction term to improving the pressure solution. $\vec{\boldsymbol{S}}'$ is the part that contributes purely to improve the discretisation accuracy of operator ψ. As such, the following equations can be obtained,

$$\vec{\boldsymbol{S}}' = -\left[\tilde{\psi}^c(\rho_{cpl}, \vec{\boldsymbol{u}}_{cpl}) - \hat{\psi}^c(\rho_{cpl}, \vec{\boldsymbol{u}}_{cpl})\right] \tag{19}$$

$$\vec{\boldsymbol{S}}'' = \hat{\nabla}^c(\chi) = -\left[\hat{\nabla}^c(\phi_{cpl}) - \hat{\nabla}^c(p_{cpl})\right]. \tag{20}$$

Equation 20 implies a simple relation between ϕ_{cpl} and p_{cpl}, that is

$$\chi = -\left(\phi_{cpl} - p_{cpl}\right) + C, \tag{21}$$

where C is a constant (C vanishes when the same reference pressure is used for ϕ_{cpl} and p_{cpl}). Obviously, key to reconstruct the real physical pressure field ϕ_{cpl} from the pressure solution p_{cpl} is to obtain the scalar field χ. Considering the fact that ϕ_{cpl} is actually an improved pressure field that is consistent with the improved velocity $\vec{\boldsymbol{u}}_{cpl}$ (see Equation 16), the gradient of ϕ_{cpl} can be approximated directly using the pressure solution of the embedded resolved model which is supposed to provide more accurate predictions in the overlapping region. In the remaining regions, the gradient of ϕ_{cpl} just stays the same as that of p_{cpl}, then the following approximation is obtained,

$$\hat{\nabla}^c(\phi_{cpl}) \approx \begin{cases} \left[\hat{\nabla}^f(p_f)\right]_c & \text{in the overlapping region} \\ \hat{\nabla}^c(p_{cpl}) & \text{in the rest of the domain} \end{cases}, \tag{22}$$

where $\left[\hat{\nabla}^f(p_f)\right]_c$ is the pressure gradient interpolated onto the coarse mesh using the pressure solution of the embedded resolved sub-model. Equation 22 is further substituted into Equation 20. Applying a divergence operation to the latter leads to a Poisson equation for the scalar field χ which can be written as follows,

$$\hat{\nabla}^c \cdot \hat{\nabla}^c(\chi) = \begin{cases} -\hat{\nabla}^c \cdot \left\{\left[\hat{\nabla}^f(p_f)\right]_c - \hat{\nabla}^c(p_{cpl})\right\} & \text{in the overlapping region} \\ 0 & \text{in the rest of the domain} \end{cases}. \tag{23}$$

Equation 23 is then solved over the entire domain with homogeneous Neumann conditions (i.e. zero normal gradient) for all boundaries. The scalar field χ can be finally determined and the interfacial discontinuities introduced in Equation 22 can be largely eliminated.

3. Validation and Application

3.1 Testing of the coupling platform using simple flow cases

To verify and demonstrate the methodology and its implementation described in Section 2, initial simulations have been carried out for two 2-D cases, including a jet flow at a T-junction (Section 3.1.1) and an external flow passing a square cylinder (Section 3.1.2). In both test cases, two-way coupling is activated and the embedded sub-model is defined over a small area only covering the most important region where the flow is expected to have complex features. In practice, a larger embedded sub-model would be recommended but the small overlapping region used here provides a more challenging test of the methodology.

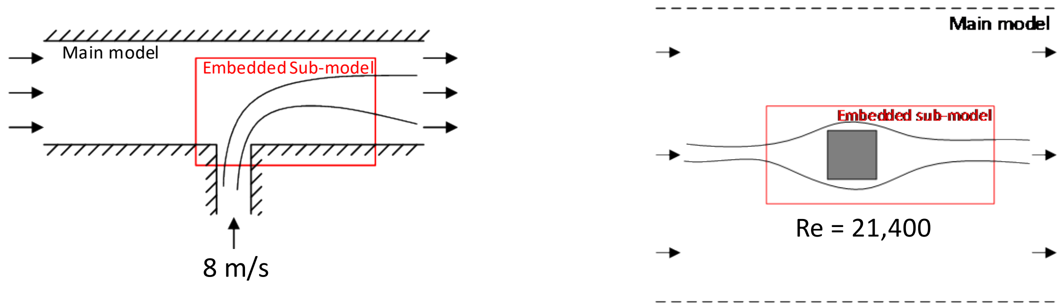

(a) (b)

Fig. 5 Initial 2-D test cases: (a) jet flow in a T-junction, (b) external flow passing a square cylinder

Figure 5 shows the arrangements of the embedded sub-models in the two test cases as well as some key flow conditions. The standard k-ε turbulence model is used in both the embedded sub-model and the coarse-grid model for both of the test cases. Dirichlet boundary conditions are used at the coupling interfaces for the turbulence variables in the embedded sub-models and they are obtained similarly to those for velocities described in Equation 6. Non-slip boundary conditions are used for all solid walls involved in the two test cases. A wall function approach is used for the near-wall modelling and the meshes are created in line with this. In each case, the results are compared with a resolved CFD model and a coarse-grid model of the entire domain, to ascertain the differences due to the coupling approach.

3.1.1 Jet flow in a T-junction

The T-junction consists of 2 branches, the main one being horizontal and 0.02 m wide and the secondary branch being vertical and 0.005 m wide. Water is used as the working fluid and the main flow in the horizontal channel is from left to right with a bulk velocity of 8 m/s. The jet is created by injecting water into the main flow through the vertical channel. The injection velocity is set to 8 m/s. The two streams strongly interact with each other around the confluence region, resulting in complex phenomena.

Figure 6 shows the meshes around the T-junction in the computational domain, including a typical resolved CFD mesh (15,800 cells) (see Figure 6a) used to produce reference CFD results and a coupled mesh system (see Figure 6b) for the coupled simulation. As can be seen, the coupled mesh system consists of a very coarse mesh (only 752 cells) covering the entire flow domain and a refined mesh (4,500 cells) covering only the confluence region. They are used in the coarse-grid model and the embedded sub-model, respectively. It should be pointed out that the refined mesh in Figure 6b has exactly the same arrangement of grid lines as that in Figure 6a. To generate fully developed inflow conditions, a mapped inlet method (that is, recycling the velocity at a cross section in the downstream of the inlet) is used for both channels. The pressure outlet condition with a fixed gauge pressure of zero is used for the outlet of the horizontal channel.

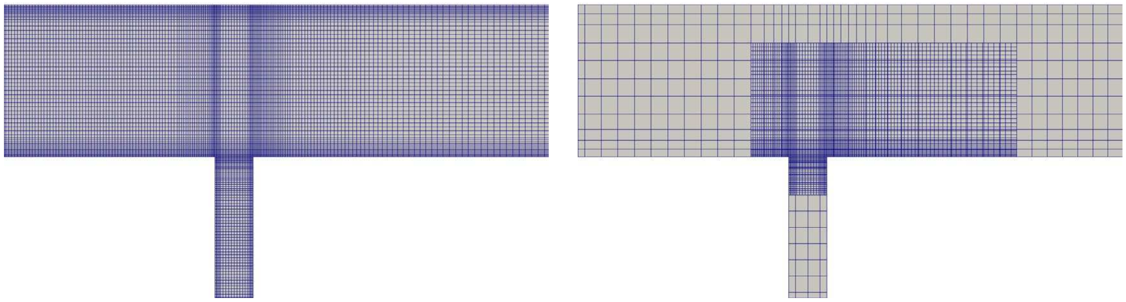

(a) (b)

Fig. 6 Meshes around the T-junction: (a) resolved reference CFD model, (b) coupled model

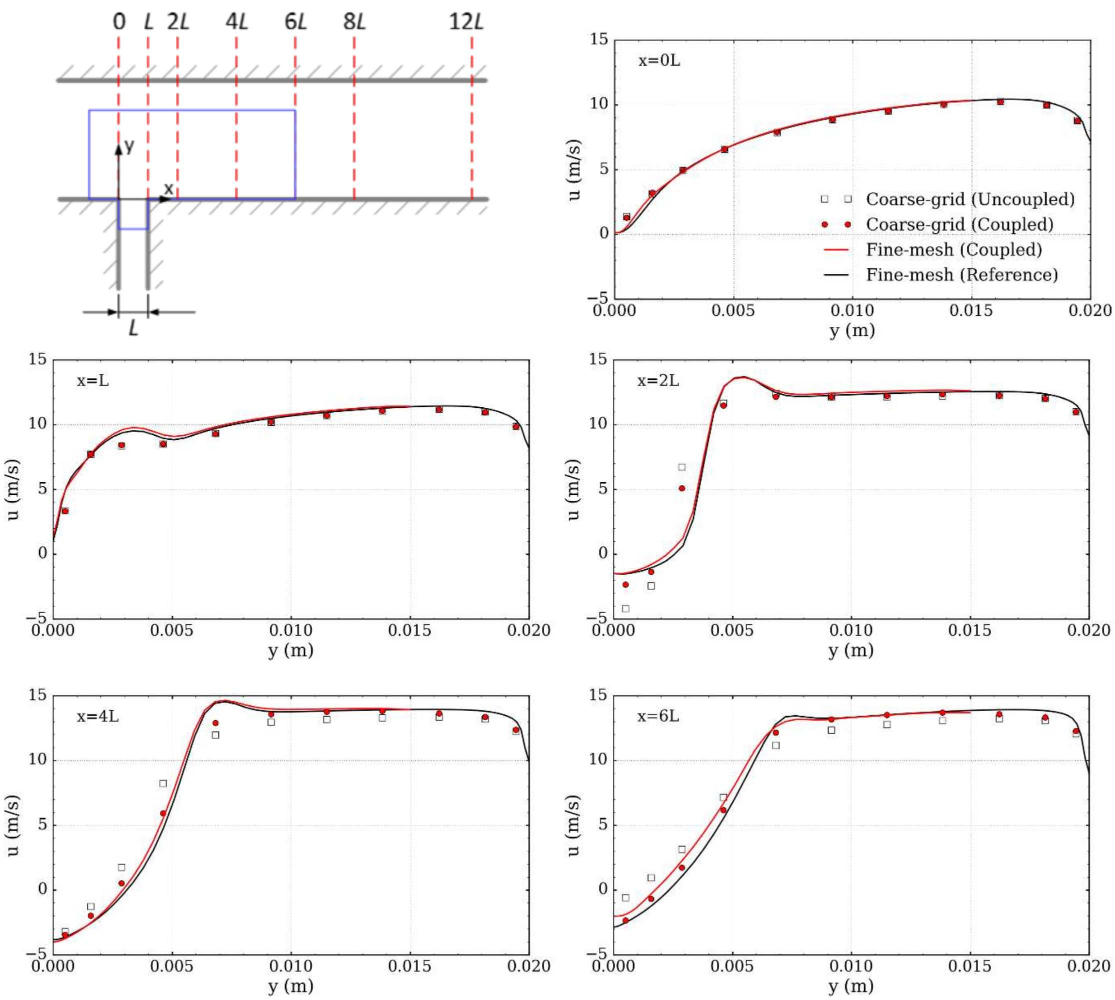

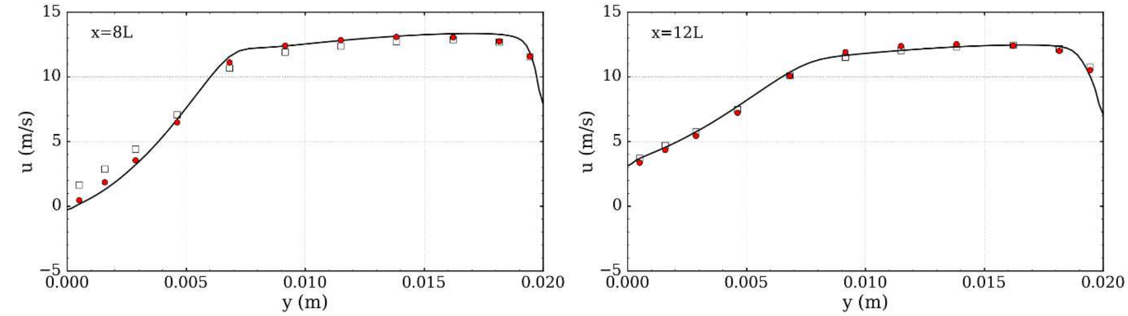

Fig. 7 Profiles of x-direction velocities at various vertical lines

Figure 7 shows the x-direction velocity profiles plotted over a series of vertical lines at different locations alone the x-axis downstream of the confluence point. Here, 'Coarse-grid (Coupled)' refers to the coarse-mesh result in the coupled simulation while 'Fine-mesh (Coupled)' refers to the embedded fine-mesh result in the same simulation. It can be seen that the coarse-mesh result in the coupled simulation is also plotted for the lines that lie outside the overlapping region (x=8L and x=12L) (see Figure 7 top left for the definition of L), to further investigate the effective zone of the coupling. Reference data are produced through a resolved CFD simulation using the fine mesh that covers the entire domain (see Figure 6a). The coarse-mesh result of an uncoupled simulation using the same coarse mesh (see Figure 6b) is also produced and plotted in these diagrams so that the improvements achieved due to model coupling can be directly evaluated.

- Without coupling, it is not surprising that the coarse-mesh result deviates greatly from the reference result due to large discretisation errors of the governing equations, especially at x = 2L, 4L, 6L and 8L (see Figure 7 top-left), where most of the complex flow features emerge. However, the situation changes when coupled with an embedded resolved model.
- Overall, the result produced by the embedded sub-model in the coupled simulation agrees very well with the reference result in all of the sampled vertical lines presented, despite some of the boundaries being placed in a very complex flow environment. It is encouraging that the coarse-mesh result is also significantly improved due to coupling, although it is not as good as its counterpart produced by the embedded sub-model. It is observed that such an improvement is not only limited to the overlapping region but also propagates beyond it, for example, at line x = 8L which sits significantly away from the embedded sub-model.

Figure 8 shows a comparison of the pressure distributions along the centre line of the horizontal channel in the T-junction. Once again, the result of the uncoupled coarse-grid model looks rather poor in terms of local distribution especially at the regions just downstream of the confluence point. This is greatly improved in the coupled simulation. It should be noted that the coarse-mesh result shown here from the coupled simulation is the reconstructed pressure ϕ_{cpl} rather than the direct pressure solution of Equation 14.

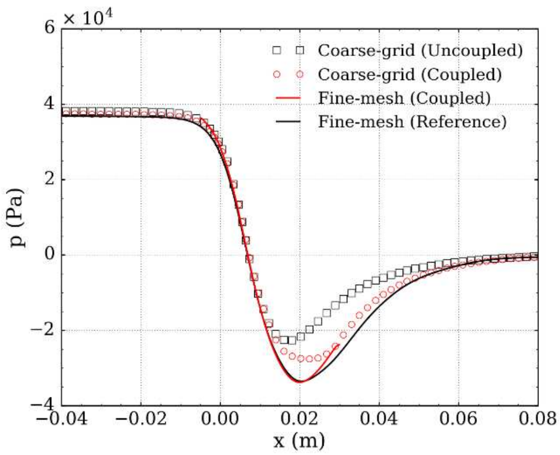

Fig. 8 Pressure distributions at the centre line of the horizontal channel

3.1.2 Flow passing a square cylinder

The second 2-D case is an external flow around a square cylinder. The cylinder is 0.04 m in width. Water at a free stream velocity of 0.535 m/s is used as the working fluid, corresponding to a Reynolds number of 21,400 (based on the width of the cylinder). Figure 9 shows the meshes used in this test case. To capture the unsteady flow behaviour, particularly the vortex shedding in the wake, a typical CFD mesh (38,240 cells) is created with careful refinement around the cylinder (see Figure 9a). However, the mesh is intentionally made very coarse for the coarse-grid model (only 1,188 cells) to further evaluate the coupling technique (see Figure 9b). As for the previous test case, the mesh for the embedded resolved model (7,080 cells) has the same grid line arrangement as that used in the reference model.

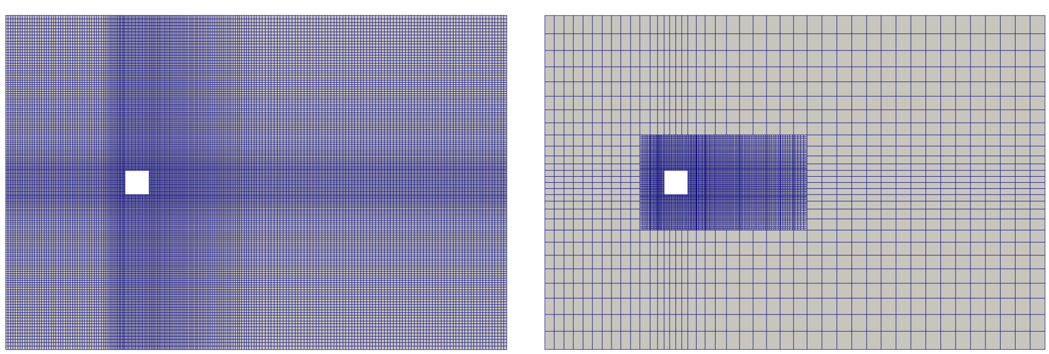

(a) (b)

Fig. 9 Meshes used in the case of flow passing a square cylinder: (a) resolved reference CFD model, (b) coupled model

The time step sizes used for the coarse-grid and the embedded resolved models are always kept the same in coupled simulations of transient problems to ensure the synchronicity of the temporal evolution of the flow in different domains. As a result, the maximum time step size used is limited by the fine-mesh domain. For simplicity, a constant time step size of 0.001 s is used for the coupled simulation in this case, which ensures the CFL criterion to be satisfied for both of the domains throughout the simulation. Considering the transient nature of the flow in this case, sub-iteration within time step is allowed to ensure convergence but leads to negeligible difference in simulation results as compared with that of a non-iterative simulation.

Simulation results are first compared between the uncoupled coarse-grid model and the resolved reference model. Snapshots of x-direction velocity contours are taken at t = 10 s when a fully developed unsteady flow has been reached after an initial transient phase. Time evolutions of the x-direction velocity component are plotted at a number of sampling points to show more details. It can be seen in Figure 10 that, for an uncoupled simulation, the coarse-grid model is unable to capture any of the important flow features let alone the details of vortex shedding. The flow predicted is nearly steady-state as indicated through the plot of time traces at the sampling points. This is not surprising because the numerical diffusion in the coarse mesh smooths out the detailed features of the flow. However, this is no longer the case in the coupled simulation. It can be seen that the flow pattern predicted by the coarse-grid model is very similar to that of the resolved reference CFD thanks to the correction source term applied, although the governing equations are still solved on the same coarse mesh. The x-direction velocity contour plotted using the result of the embedded resolved sub-model is also shown in Figure 10 (in the bottom left sub-figure) with the coarse-mesh result displayed in the background. In both results, the oscillating wake is successfully reproduced and the main flow structure is well represented.

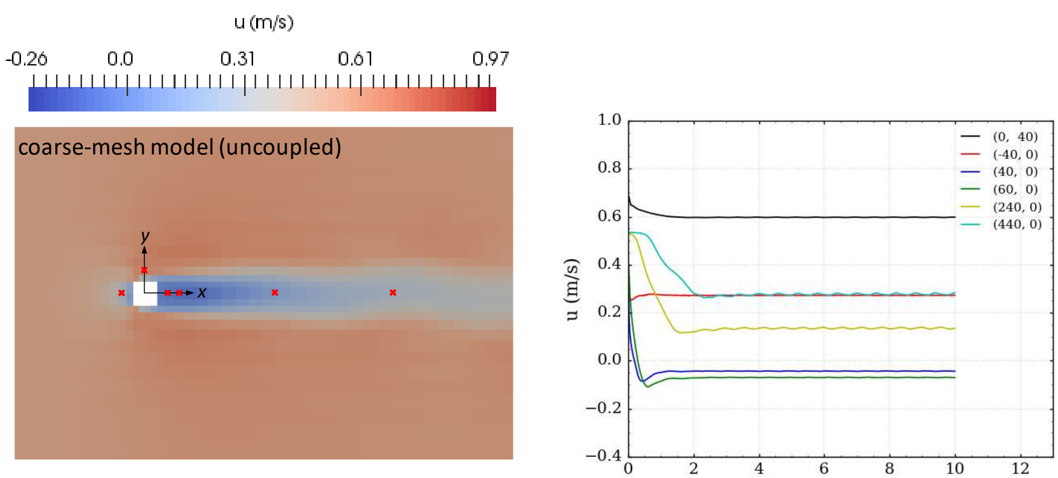

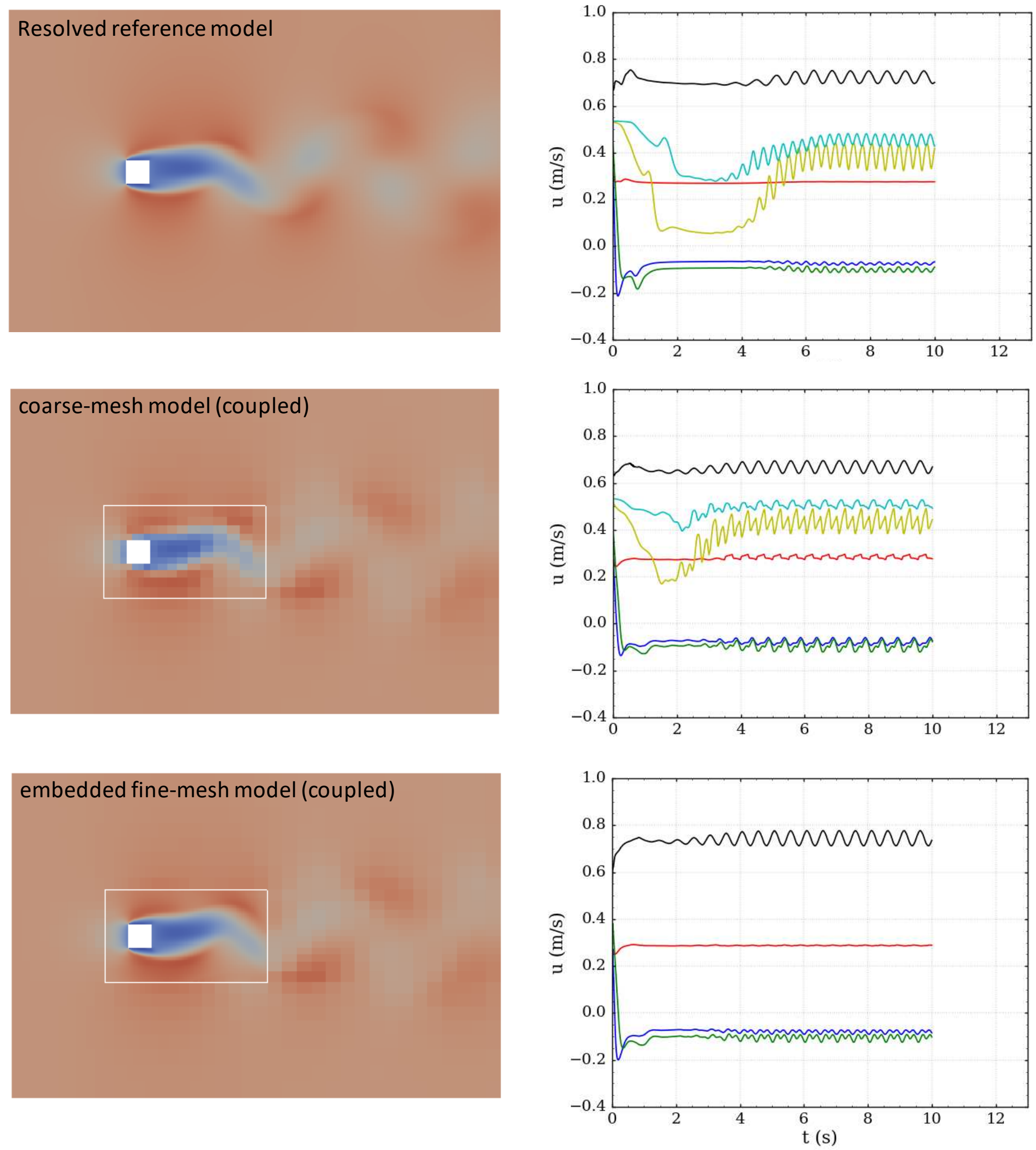

Fig. 10 Comparison of the flow fields between the coupled and the uncoupled simulations. Left column: x-direction velocity contours at t = 10 s, Right column: history of the local velocity development at sampling points shown in the left top sub-figure

Table 2 shows a comparison of the predicted Strouhal number between the coupled simulation and the reference CFD. The transient behaviour produced in the coarse-grid model is a direct result of the correction source term passed back from the embedded sub-model in the coupled simulation, hence an identical Strouhal number of 0.146 is obtained in the two coupled models, which is very close to that obtained in the reference CFD simulation. Nevertheless, it is worth noting that the initial evolution of the flow predicted by the coarse-grid model in the coupled simulation differs from that of the reference results. This may be due to the complex interactions between the coupled models in transient flow simulations. For example, the coupling errors arising from interpolation between different meshes, may not only spread in space but also accumulate in time, which poses additional challenges to the methodology in question. To further improve the results in transient flow simulations, it is suggested that a relatively large domain is used for the embedded sub-model to avoid its boundaries being defined at locations where the flow is still very complex, especially in terms of temporal variations. For such simulations, using a small correction factor (normally smaller than 0.1) can help to suppress numerical instabilities.

Table 2 Strouhal numbers obtained from the simulations

Cases	Coupled coarse-grid	Coupled embedded	Resolved reference
Strouhal number	0.146	0.146	0.131

3.2 Applications in rod bundle flows

With sufficient confidence gained from the initial tests, the coupling method is ready to be used in simulating complex flows in realistic reactor rod bundle configurations. In this section, two 3-D rod bundle cases are selected to carry out the tests. The first one is taken from the work of Creer and co-authors (Creer et al., 1979), who carried out an experimental study to investigate the turbulent flow phenomena near postulated sleeve blockages in a 7×7 model nuclear fuel rod bundle. The blockages are characteristic of fuel clad 'ballooning' or 'swelling' which could occur during a LOCA accident of a PWR. Because of the strong deformation of the fuel rod, the flow profile across the blockage may be strongly distorted compared with that in normal sub-channel configurations, which poses challenges to standard SubChCFD.

The second test case is a 5×5 PWR rod bundle with a lateral jet flow at one corner of the housing walls. The configuration used follows the one used in the study of Bieder and Rashkovan (2019) who used Large Eddy Simulation (LES) to study complex cross flows in the so-called baffle jetting phenomenon which may happen in real life PWR reactors. Such reactors are usually designed with a counter flow configuration in the core bypass region where baffle plates are placed between the core and the core barrel to allow a bypass flow of the coolant. Cross flows through the enlarged baffle gaps may happen when a significant pressure difference is established between the two sides of the baffle plates, leading to a high speed jet towards the fuel rods in the core. Such a phenomenon is obviously beyond the modelling capability of standard SubChCFD.

3.2.1 Flow blockage in a postulated ballooned 7×7 PWR rod bundle

In Creer's experiment, the rod bundle was unheated and the blockages were positioned on the central nine rods, resulting in a maximum of 70% area reduction of the centre four sub-channels. Water at 29.4 °C was used as the working fluid in the experiment. A bulk velocity of w_0 = 1.74 m/s was used away from the blockage region, corresponding to a Reynolds number of 2.9×10^4 (based on the hydraulic diameter of the non-damaged rod bundle geometry). Axial velocities and their fluctuations were measured at various locations of the rod bundle, which can be used for validation purpose.

Like the 'standard' RANS approach, there are also considerable flexibility in setting up the SubChCFD model and computational domain. In this case study, a SubChCFD model is created based on ¼ sector of the entire geometry to take advantage of the symmetries in the rod bundle structure and the flow. Accordingly, an embedded resolved sub-model, covering the 4 sub-channels adjacent to the ballooned fuel rods, is created for the coupled simulation. Geometrical details of these models can be found in Figure 11, in which the sizes and locations of the embedded sub-domain are highlighted using red dash lines.

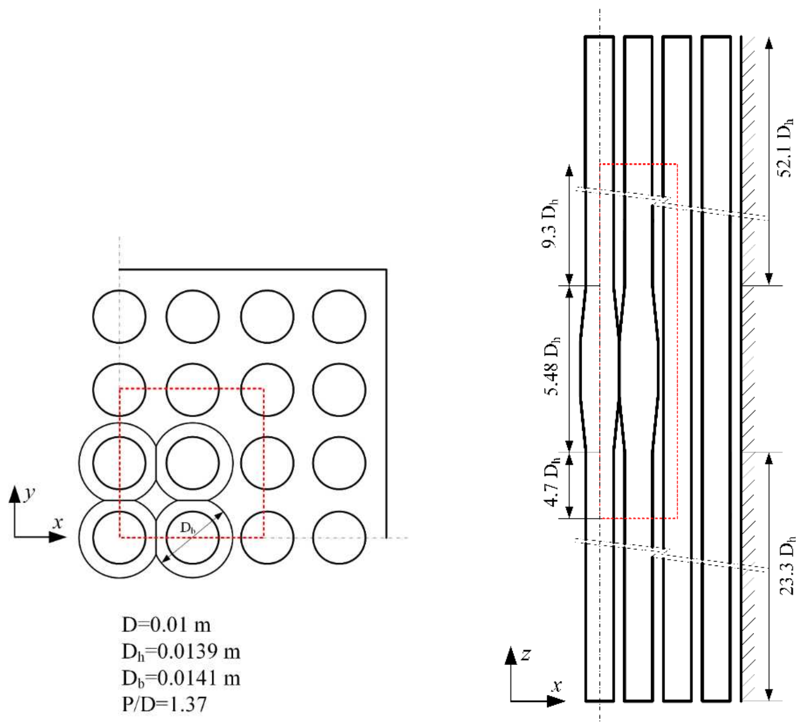

(a) (b)

Fig. 11 Geometry used in the coupled simulation for the 7×7 ballooned rod bundle case: (a) top view of the model (the ¼ sector of the rod bundle), (b) side view of the model

Figure 12 shows clipped views of the meshes used for the relevant models and sub-models. A meshing scheme that is equivalent to scheme 1 type of mesh defined in Liu et al. (2019) is used for the coarse mesh generation, which leads to a total number of 0.11 million hexahedral cells. The meshing scheme used for the embedded sub-model for the overlapping region is overall in line with the use of a wall function approach (except for the narrow gaps around the blockage), and the resulting mesh consists of 0.1 million cells. As such, the total number of mesh cells in the coupled simulation is 0.21 million. A refined mesh for the complete domain has also been generated for resolved CFD simulation to produce reference data (shown in Figure 12c). This mesh has a the same resolution as that of the embedded sub-model, consisting of about 1.6 million cells. As expected, such a coupling only leads to a slight increase in computing cost compared with an uncoupled SubChCFD simulation. Table 3 gives the CPU times of the relevant simulations conducted for this case. Compared with a conventional resolved CFD approach, the computing cost in the coupled simulation is reduced by more than 80%.

A modified Launder-Sharma k-ε model is used in combination with an all-y^+ wall function to describe the turbulent flow in both the embedded sub-model in the coupled simulation and the reference resolved CFD model. Unlike a standard low Reynolds number approach, such a strategy does not have a stringent requirement that the near-wall meshes are refined consistently down to the viscous sub-layers, thus ensuring a relatively low computing cost. For the narrow gaps around the blockage where the mesh is somewhat 'over-refined', the model reduces automatically into a standard low-Reynolds treatment. For the regions away from the blockage where the mesh may be less refined, the model switches smoothly into a wall function approach with the increase of the dimensionless wall distance y^+ of the first layer of cells through a blending function (Code_Saturne development team, 2019).

For the sake of simplicity, the same turbulence model is used for the coarse-grid SubChCFD model to allow a straightforward coupling with the embedded resolved sub-model. It should be pointed out that it is not necessary for the turbulence models used for the coupled models to be the same. In practice, turbulence models used for the embedded sub-model should be selected with caution so that flow physics can be captured correctly. However, turbulence models play a lesser important role in SubChCFD since it is only active in the core flow region of the sub-channels.

Table 3 Mesh sizes and CPU times of relevant numerical models

Numerical models	Uncoupled SubChCFD	Coupled SubChCFD	Resolved CFD
Mesh size (million cells)	0.1	0.21	1.6
CPU time per iteration (s)	7.29	12.48	71.64

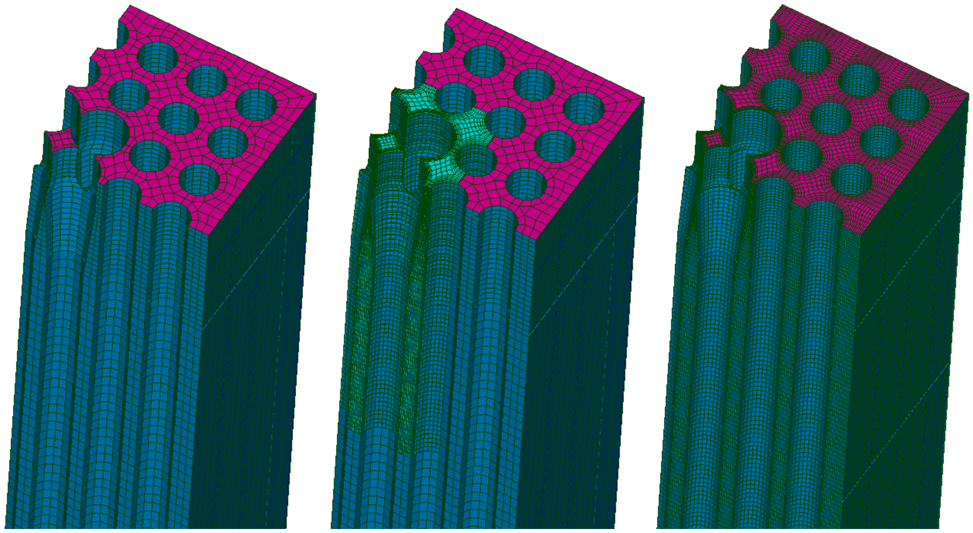

(a) (b) (c)

Fig. 12 Clipped views of meshes used for the 7×7 rod bundle case: (a) coarse-grid SubChCFD model, (b) coupled simulation model, (c) resolved reference CFD model (the horizontal clipping plane is located at the centre of the blockage)

Simulation is first performed using SubChCFD alone. Results obtained are compared with both the reference CFD solutions and the experimental data wherever available. Figure 13a shows the axial velocity distribution along the centre line of the central blocked sub-channel. Significant errors occur downstream of the blockage where the recovery of the reduced axial velocity in the wake is severely under-predicted, indicating that the inter-channel mixing is underestimated. Through coupling with an embedded resolved model (see Figure 12b), the simulation results are improved both in terms of capturing the peaks and the distribution. Clearly, the improvements are not limited to the model overlapping region, but 'travel' with the flow downstream in the wake due to the convective effect.

Figure 13b shows the axial pressure distribution along the centreline of the central blocked sub-channel. Since no experimental data are available for pressure, the result of the resolved CFD model is considered as the only reference. It can be seen that some details of the pressure distribution, especially those across the blockage, are poorly predicted when using SubChCFD alone, although the overall head loss is correct. In contrast, such details are relatively well captured by the embedded resolved model in the coupled simulation, despite some discrepancies in the regions immediately downstream of the blockage. It is encouraging that the reconstructed pressure of the SubChCFD model in the coupled simulation is rather good, which follows very closely the reference result, reproducing nearly every detail of the pressure field development.

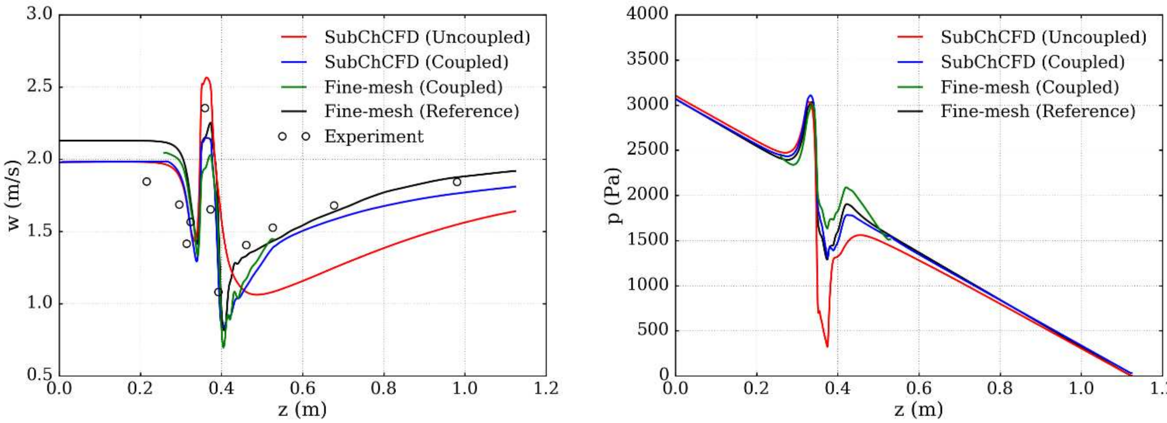

(a) (b)

Fig. 13 Simulation results plotted along the axial centreline of the central blocked sub-channel: (a) axial velocity, (b) pressure

Figures 14 and 15 show the distributions of the axial velocity component on the cross sections normal to the z-axis. Two planes are selected to present the results, one of which is located at 1.462D_h (D_h is the hydraulic diameter of a non-damaged rod) upstream of the centre of the blockage (Figure 14), and the other is located at 2.559D_h downstream of the centre of the blockage (Figure 15). It can be seen that, in the coupled simulations, the results of the embedded sub-model agree very well with the reference results provided by the resolved CFD simulations in the centre four sub-channels. Besides, the results of the SubChCFD model are also improved consistently over these regions due to the use of the two-way coupling. This is especially significant for the results shown in Figure 15, in which the uncoupled SubChCFD simulation severely underestimated the axial velocity in the two sub-channels adjacent to the central blocked sub-channel.

Figure 16 shows more details of local velocity profiles, which covers four different axial locations, that is, $z = -1.462D_h$, $z = 1.462D_h$, $z = 2.559D_h$ and $z = 3.655D_h$ ($z = 0$ represents the centre point of the blockage). Each of them is plotted over the blue straight line shown in the embedded picture of Figure 16b. Comparisons are not only made between simulation results but also with available experimental data for better validation. It is not surprising that the reference CFD model produces the closest results to the experiment, capturing the basic trend of velocity profile distortion caused by the blockage, despite some deviations in the regions near the centre of the blockage. Such deviations may be caused by the inaccuracy of the turbulence model or the wall function used. Nevertheless, this will not affect the effectiveness of the resolved CFD result to be used as a reference in evaluating the coupling approach. Moreover, the current study is aimed at demonstrating methodology rather than pursuing accurate numerical results.

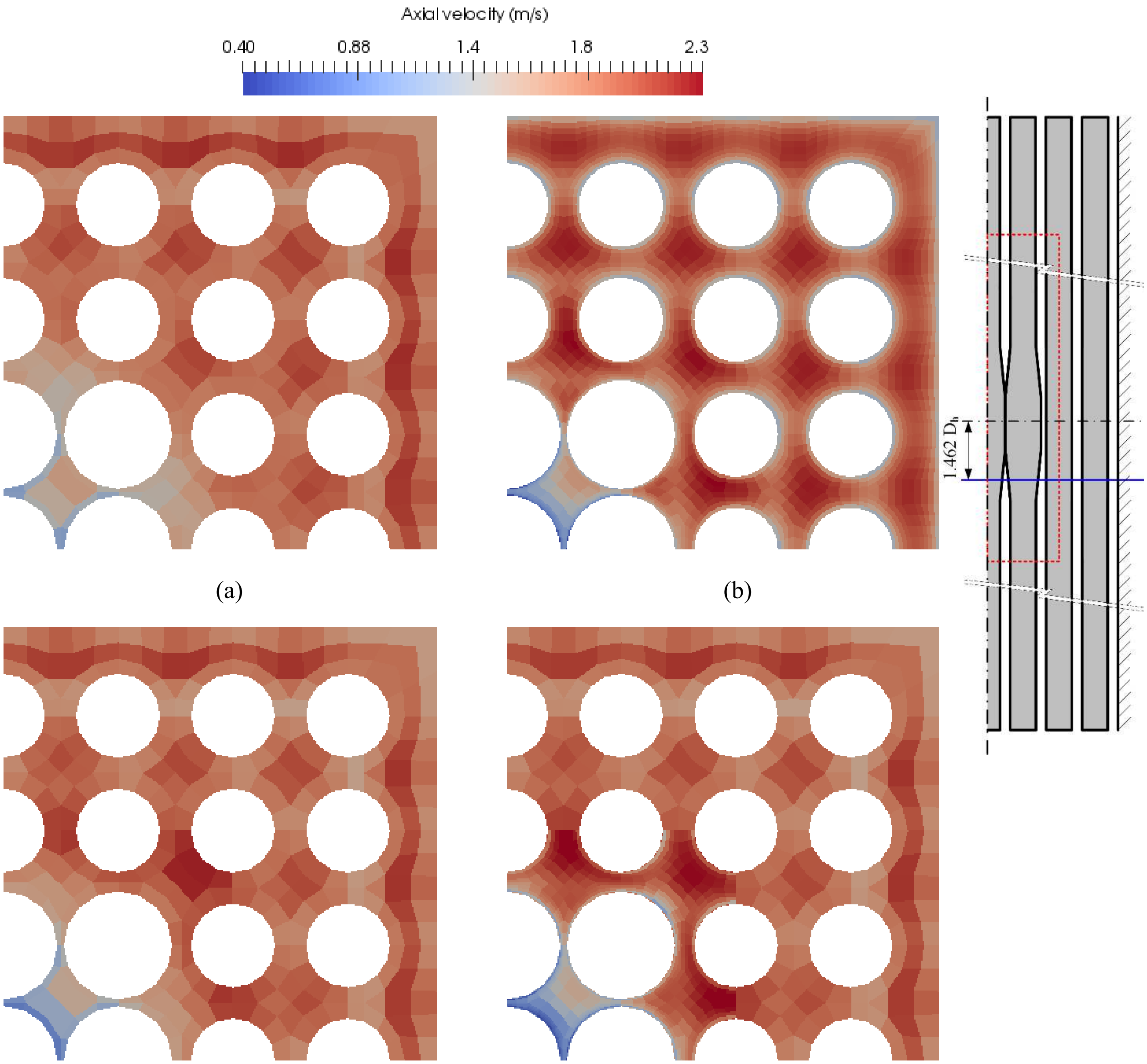

(c) (d)

Fig. 14 Contour plots of the axial velocities at a horizontal plane located 1.462D_h upstream of the centre of the blockage: (a) SubChCFD result in an uncoupled simulation, (b) reference resolved CFD result, (c) SubChCFD result in a coupled simulation, (d) embedded model result with the SubChCFD result in the background

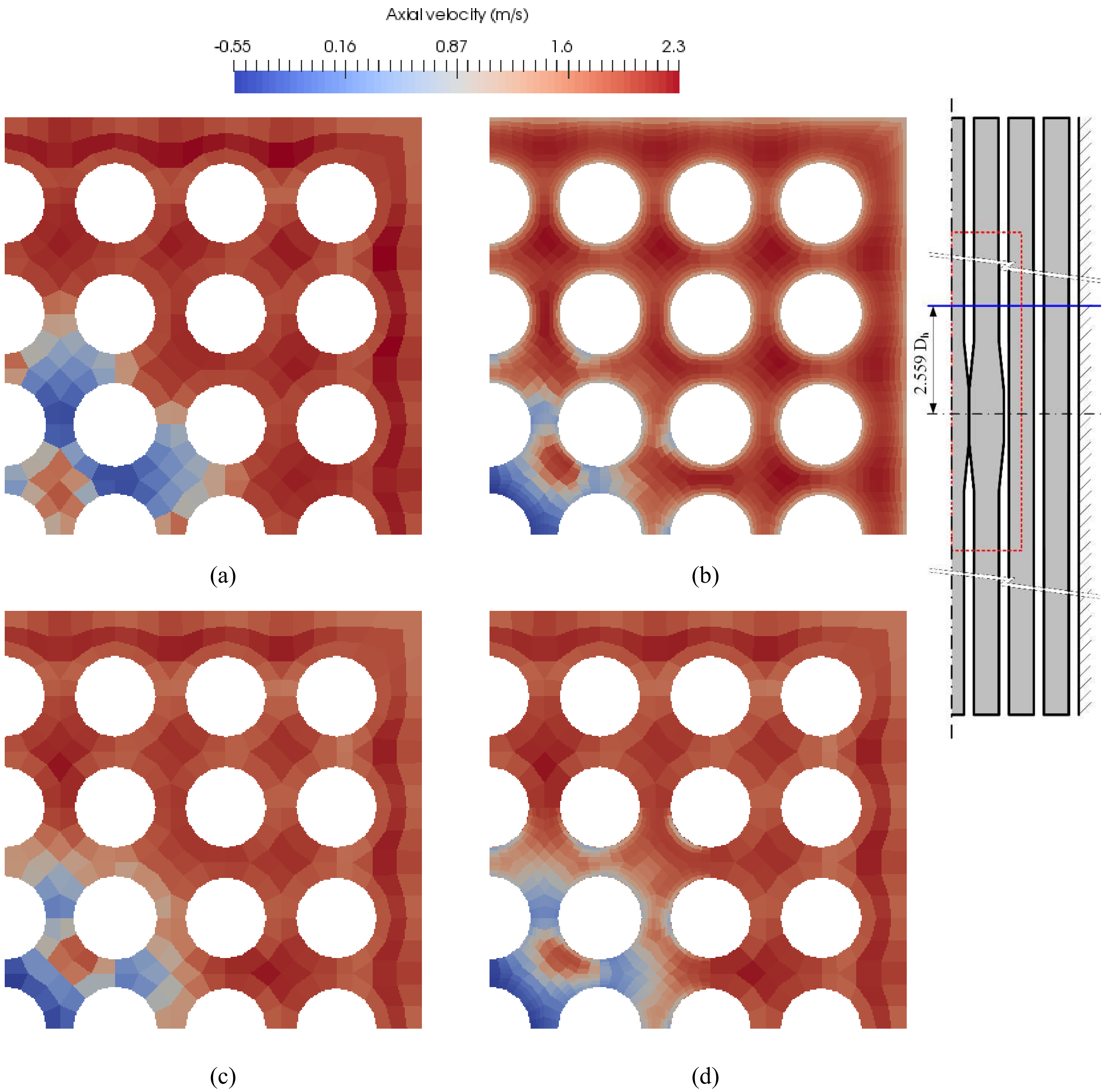

Fig. 15 Contour plots of the axial velocities at a horizontal plane located 2.559D_h downstream of the centre of the blockage: (a) SubChCFD result in an uncoupled simulation, (b) reference resolved CFD result, (c) SubChCFD result in a coupled simulation, (d) embedded model result with the SubChCFD result in the background

Again, it can be seen more clearly from Figure 16 that the results of the coupled simulation (including both the embedded sub-model and the SubChCFD model) are closer to the reference results than those of the uncoupled SubChCFD simulation. It is worth pointing out that such results are obtained using a relatively small embedded sub-domain which only covers four sub-channels around the blockage. It is expected that the coupled simulation will converge to the reference resolved model when the embedded sub-domain is appropriately enlarged, for example, to cover nine sub-channels around the blockage. In practice, users can conduct a set of trial simulations to finally determine the best size and location of the embedded sub-domain to balance the requirement in accuracy and the computing cost.

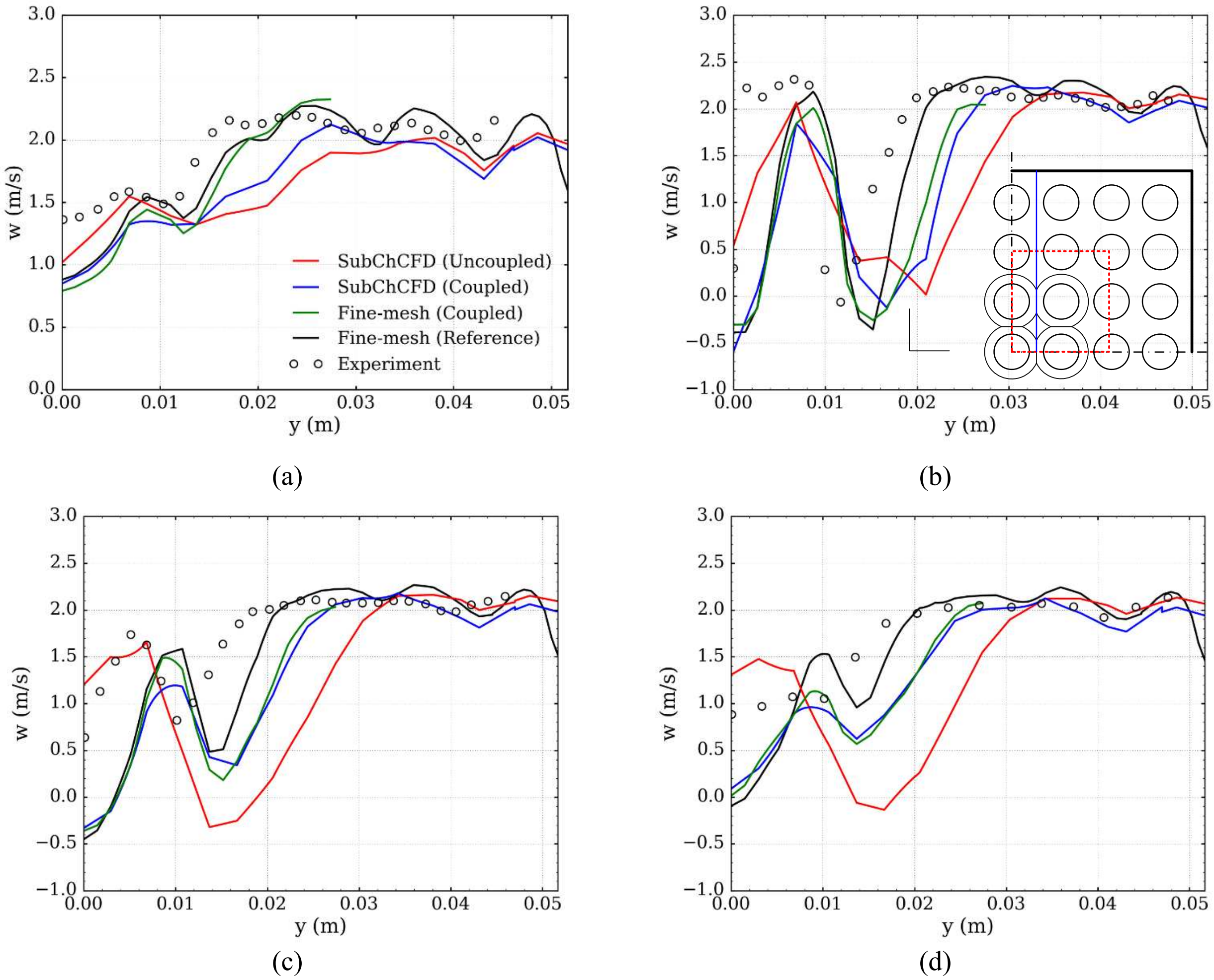

Fig. 16 Comparisons of the axial velocity between the coupled and uncoupled simulations: (a) 1.462D_h upstream of the centre of the blockage, (b) 1.462D_h downstream of the centre of the blockage, (c) 2.559D_h downstream of the centre of the blockage, (d) 3.655D_h downstream of the centre of the blockage

3.2.2 Baffle jetting in a 5×5 PWR rod bundle

Bieder and Rashkovan (2019) extended their simulation model for a rod bundle from 5×5 to 6×6 and found the location of the farther boundary has negligible influence on the jet. Consequently, the 5×5 configuration has been chosen to be used to simulate the baffle jetting phenomenon of a PWR. Figure

17a is a cross-sectional view of the 5×5 rod bundle. The top and right boundaries of the rod bundle are made symmetric to represent that this is a portion of a real-life PWR fuel assembly. The left and bottom boundaries are non-slip solid walls, which is to mimic the corner baffle plates in the core. Between the two perpendicular baffle plates, a 0.001 m gap is left to allow a high-speed inward cross flow into the core to simulate the baffle jetting. In the simulation, a 5 m/s input velocity has been imposed at the gap to create the jet flow. Figure 17a also shows some other key dimensions of the rod bundle, which are obviously similar to a real PWR.

Figure 17b is a side view of the 5×5 rod bundle. The length of the rod bundle is 0.5 m, and the baffle plate gap starts at the location 0.012 m downstream of the inlet plane and ends at the outlet plane of the rod bundle. To obtain a fully developed flow profile at the inlet, the computational domain of the rod bundle is extended from the inlet plane along the axial direction by several times of the hydraulic diameter to allow a mapped inlet approach to be used. The working fluid used in this simulation is water at 330 ℃ and 15 MPa, which leads to a density of 644 kg/m^3 and a dynamic viscosity of 7.5×10^{-5} Pa·s. The bulk velocity at the inlet of the rod bundle is 5.35 m/s, and the corresponding Reynolds number is 5.41×10^5 (based on the hydraulic diameter of the inlet channel).

To capture the localised complex flows arising due to the baffle jetting using the SubChCFD modelling, an embedded resolved sub-model is created for the highlighted region (in red colour) in Figure 17 so that a coupled modelling system can be finally set up. The resolved sub-model covers two ranks of the sub-channels adjacent to the jet, starting from an axial location where the gap starts and covers a length of 0.21 m downstream. In practice, users can adjust the position and size of the embedded sub-domain according to their needs.

Figure 18 shows the meshes used in the test simulations. Figure 18a is the coarse mesh for SubChCFD, which is in line with the coarsest mesh (meshing scheme 1) used in Liu et al. (2019), leading to a total number of 0.14 million cells. The coarse mesh has been slightly refined at the corner sub-channel where the jet is located so that the velocity inlet boundary condition can be accurately imposed. Figure 18b is the fine mesh used for the resolved CFD reference model which consists of 25.6 million cells. Some details of the mesh are better shown in Figure 18c. It should be clarified again that the mesh used for the embedded sub-model (consisting of 3.9 million cells) in the coupled simulation is exactly the same as that of the resolved reference model that covers the complete domain in the regions where they overlap, and hence it is not shown here.

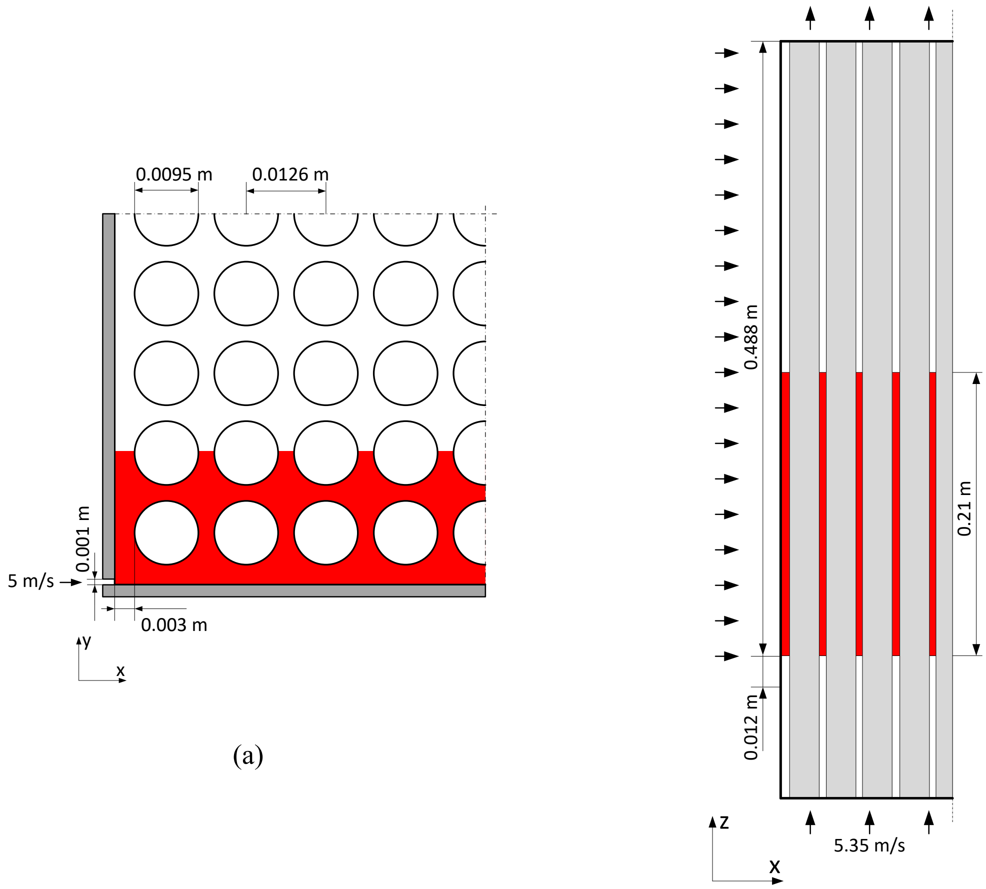

(a) (b)

Fig. 17 Geometry used in the coupled simulation for the 5×5 rod bundle case: (a) cross-sectional view of the domain, (b) side view of the domain (the embedded sub-domain is highlighted in red)

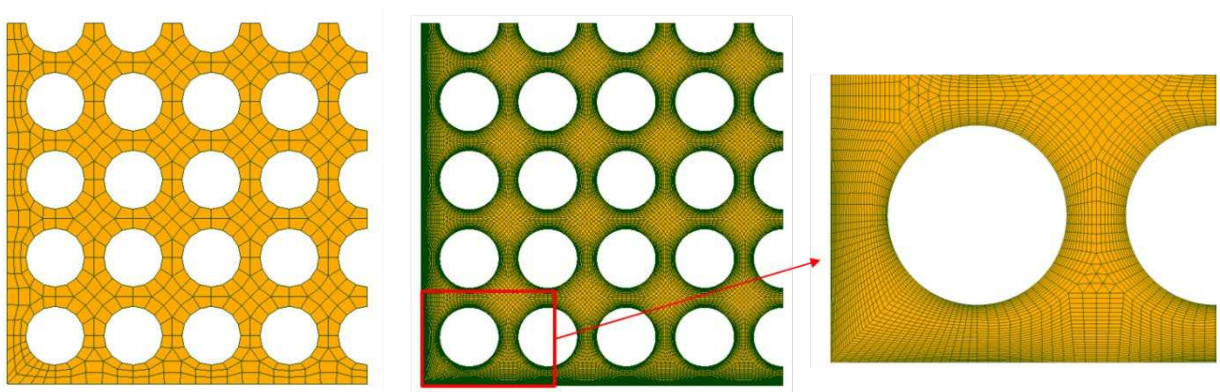

(a) (b) (c)

Fig. 18 Cross-sectional view of meshes in the 5×5 rod bundle case: (a) SubChCFD mesh, (b) resolved CFD mesh (c) local zoom-in of the resolved CFD mesh

Figures 19 and 20 show the distributions of the z-direction velocity component on the cross sections normal to the z-axis. The locations are 0.03 m and 0.1 m downstream from the start of the jet, respectively. Both figures show that the distortion of the velocity profile caused by the jet flow is well captured in the coupled simulation compared with that of the resolved reference results, but this cannot be achieved by using SubChCFD alone.

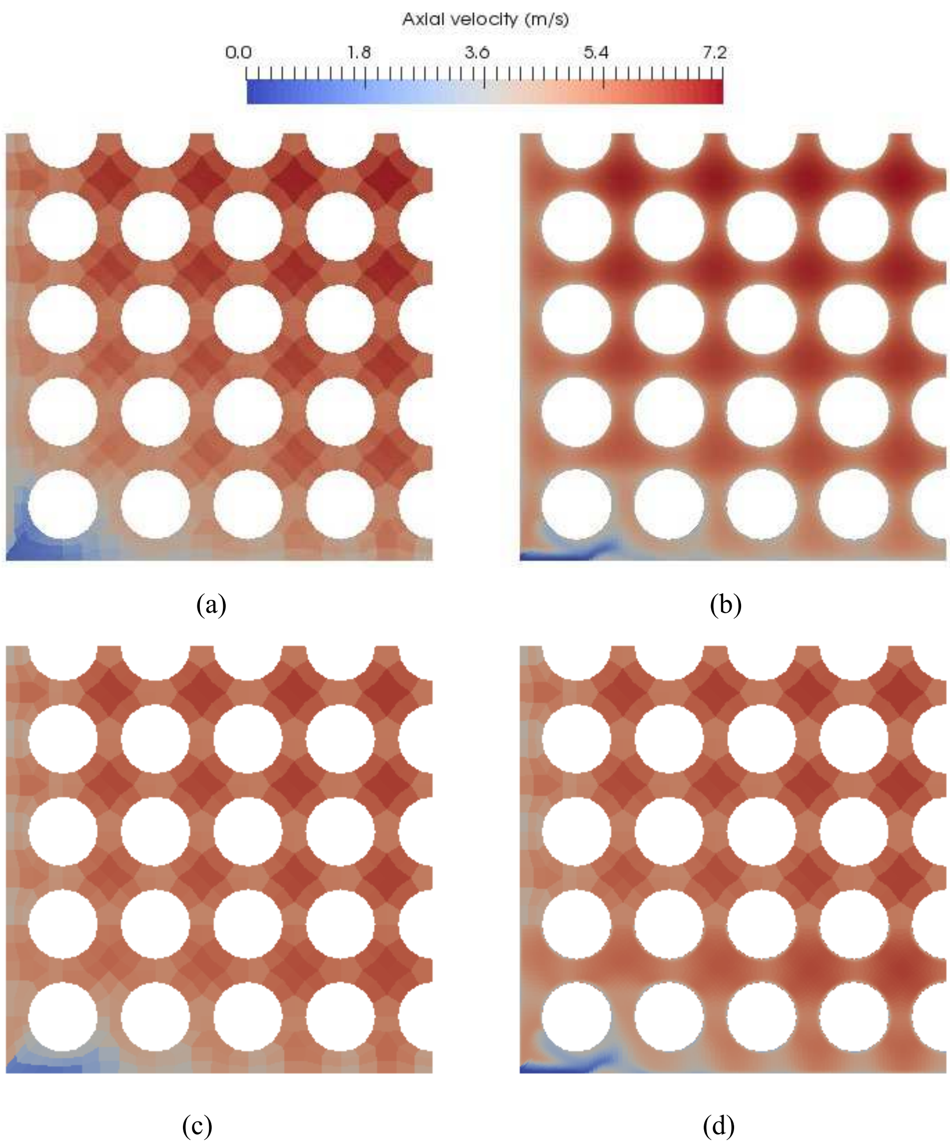

Fig. 19 Contour plots of the axial velocities at a horizontal plane located 0.03 m downstream of the start point of the jet: (a) SubChCFD result in an uncoupled simulation, (b) reference resolved CFD result, (c) SubChCFD result in a coupled simulation, (d) embedded model result with the SubChCFD result in the background

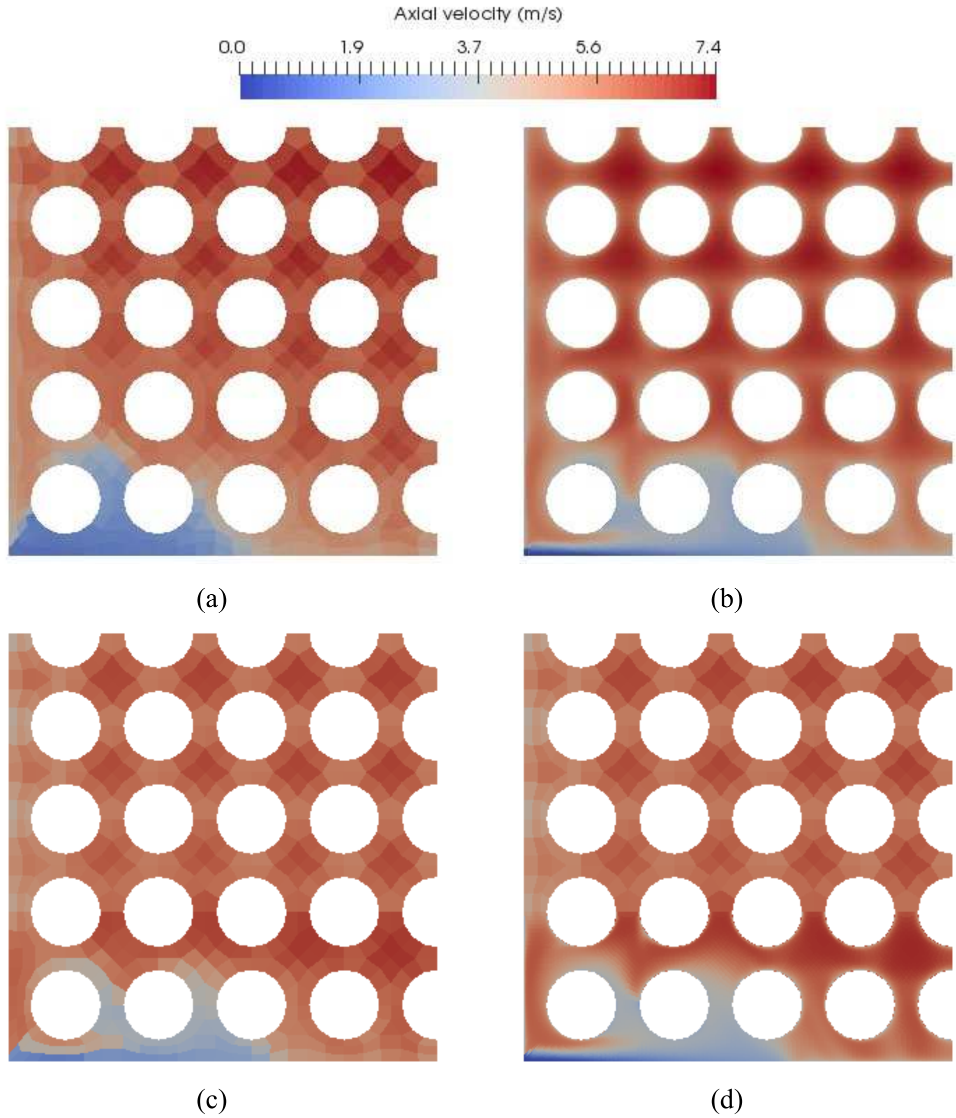

Fig. 20 Contour plots of the axial velocities at a horizontal plane located 0.1 m downstream of the start point of the jet: (a) SubChCFD result in an uncoupled simulation, (b) reference resolved CFD result, (c) SubChCFD result in a coupled simulation, (d) embedded model result with the SubChCFD result in the background

Figure 21 shows the velocity distribution in a vertical plane that is oriented in parallel to the bottom baffle plate shown in Figure 17a. The plane is also located passing through the centre of the gap. It can be seen that a narrow low velocity zone is predicted by the resolved reference model, separating the jet flow region and the axial mainstream of the flow, which is one of the most significant features in the baffle jetting phenomenon. Such a feature is successfully captured by the coupled simulation but cannot be captured by the uncoupled SubChCFD model which significantly mis-predicts the low velocity zone and fails to capture the high velocity region close to the start of the jet. This is more clearly shown in the line plots of Figure 22. In addition, the velocity vector field predicted by the coupled simulation looks more consistent with the reference result in terms of magnitudes as well as flow directions. However, it should be noted that the velocity magnitude in the main stream of the flow (i.e. the region where the flow is not directly affected by the jet) is over-predicted in the coupled simulation compared with the resolved reference result. This may be due to the inflow effects in the resolved sub-model and can be alleviated by extending the inlet section of the embedded sub-domain (note that the velocities of the coarse mesh used to define the near wall velocities of the fine mesh at the inlet are over-estimated due to the significant discrepancy in mesh resolution between the coupled models).

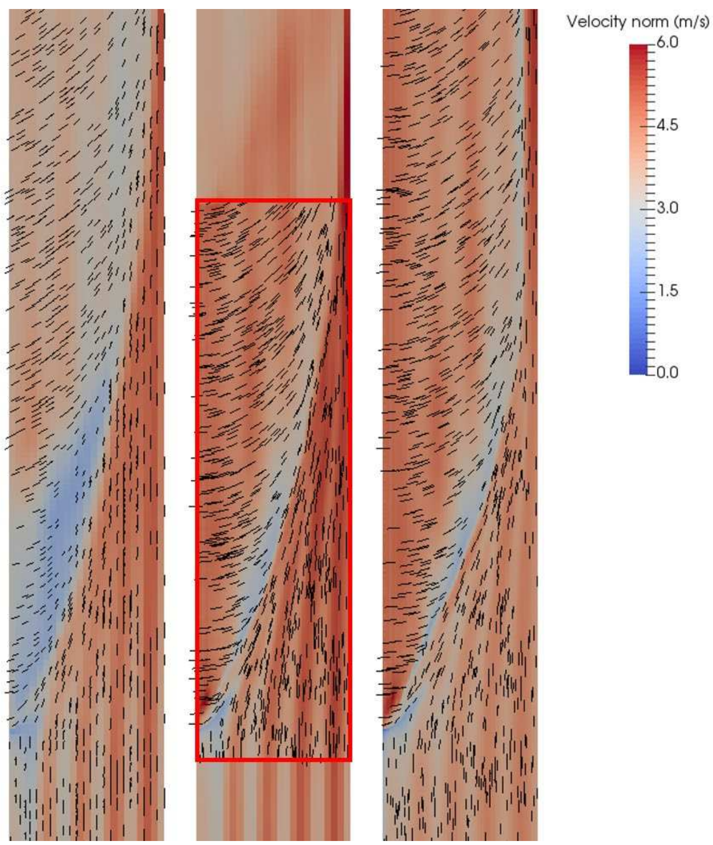

(a) (b) (c)

Fig. 21 Velocity magnitude and vector field in a vertical plane that is in parallel to the bottom baffle plate and passing through the centre of the gap: (a) SubChCFD results in an uncoupled simulation, (b) simulation results of the coupled simulation, (c) reference resolved CFD results

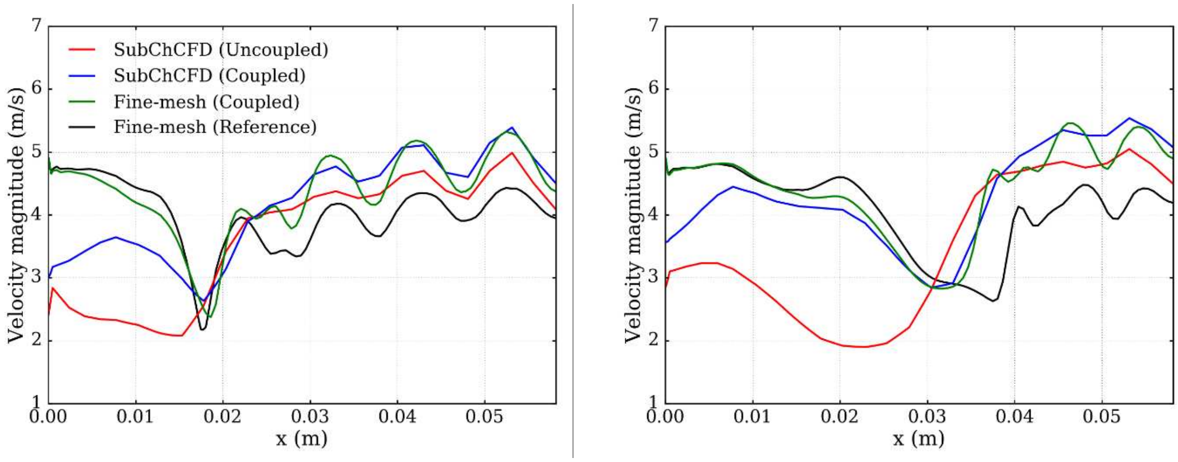

(a) (b)

Fig. 22 Line plots of the velocity magnitude along the x-axis in the vertical plane shown in Figure 21 at two axial locations downstream of the start point of the jet: (a) 0.05 m, (b) 0.1 m

4. Conclusions

A time-explicit domain overlapping method to couple SubChCFD and locally embedded resolved CFD models has been developed and implemented, which enables a flexible refinement of the coarse mesh solution. In the coupling system, the SubChCFD model covers the entire domain to be simulated and has all boundary conditions defined, so that it can be solved independently. Conversely, the embedded resolved sub-model needs to gain information from the coarse-grid model to define its boundary conditions at the coupling interfaces. Dirichlet-type conditions are used for these interfaces on which the variables to be defined are calculated using the information from both the coarse mesh and the fine mesh to ensure good numerical stability.

Both one-way and two-way couplings are possible. The latter can be enabled by allowing feedback from the embedded resolved sub-model to the coarse-grid model. This feature is aimed at improving the simulation results of the coarse-grid model in complex flow situations. A correction source term is added to the momentum equation solved in the coarse-grid model to force the solution to approach that of the embedded resolved sub-model. The calculation of the correction source term is based on the local velocity difference between the coupled models and as such is straightforward.

The methodology has been first tested using simple 2-D cases, including a jet flow in a T-junction and an external flow passing a square cylinder. Through comparisons with reference CFD results, the two-way coupling has been found to significantly improve the coarse mesh results both in the velocity and the pressure fields. Next, the coupling method was used to simulate 3-D complex flows in nuclear rod bundle configurations, including a 7×7 rod bundle with local fuel rod ballooning and a 5×5 rod bundle with a corner baffle jetting. In both cases, a refined sub-model was embedded into the baseline SubChCFD model to account for the complex flow phenomena induced by the distortion of the geometry (the 7×7 rod bundle case) or a strong cross flow (the 5×5 rod bundle case). Compared with solutions using SubChCFD alone, the coupled simulations consistently produce more accurate results at a price of a small increase in computing cost.

Future work will include the development of the capability in handling heat transfer and improvement of the robustness for transient problems.

Nomenclature

C	An integration constant in Equation 21, Pa
D	Diameter of the fuel rod in a rod bundle, m
D_b	Maximum diameter of the ballooned fuel rod in the 7×7 rod bundle, m
D_h	Hydraulic diameter of a rod bundle, m
f	Skin fractional factor
$\vec{\boldsymbol{J}}$	Convective mass flux, kg/m^2·s
$\vec{\boldsymbol{n}}$	Unit normal face vector of a cell face
p	Pressure, Pa
P	Pitch of a rod bundle, m
$\vec{\boldsymbol{S}}_M$	General source term of the momentum equation, N/m^3
$\vec{\boldsymbol{S}}'$	Effective part of the correction source term, N/m^3
$\vec{\boldsymbol{S}}''$	Potential part of the correction source term, N/m^3
$\vec{\boldsymbol{S}}_\Delta$	Correction source term in the momentum equation of the coarse-grid model in a two-way coupled simulation, N/m^3
S	Surface area of a cell face, m^2
t	Time, s
Δt	Time increment, s
$\vec{\boldsymbol{u}}$	Velocity vector, m/s
x, y, z	Spatial coordinate, m

Greek Letters

δ	Kronecker delta
λ	Relaxation factor in the correction source term
μ	Molecular viscosity, Pa·s
μ_t	Eddy viscosity in a RANS momentum equation, Pa·s
ρ	Density, kg/m^3
$\overline{\overline{\sigma}}$	Stress tensor, Pa
ϕ	Reconstructed pressure defined in Equation 16, Pa

χ	Potential of vector field $\vec{\boldsymbol{S}}''$, Pa
ψ	Operator defined as $\psi(\rho,\vec{\boldsymbol{u}}) = \nabla\cdot(\rho\vec{\boldsymbol{u}}\otimes\vec{\boldsymbol{u}}) - \nabla\cdot(\mu_{eff}\nabla\vec{\boldsymbol{u}}) - \vec{\boldsymbol{S}}$
$\hat{\psi}$	Discrete form of operator ψ
$\tilde{\psi}$	Unknown discrete form of operator ψ
Ω	Cell volume in a FV approach, m^3

Superscripts

n	Time step n
$n+1$	Time step n+1
c	Discrete operators related to a coarse mesh
f	Discrete operators related to a fine mesh

Subscripts

b	Sub-channel bulk quantities Sub-channel bulk quantities
c	Variables defined on a coarse mesh in an uncoupled simulation
f	Variables defined on a fine mesh in an uncoupled simulation
cpl	Variables defined on the coarse mesh in a coupled simulation
i, j, k	Indices of spatial coordinates
dis	Variables defined on the distant mesh in a coupled mesh system
loc	Variables defined on the local mesh in a coupled mesh system

Acknowledgements

The present work was carried out as part of the R&D Program for Digital Reactor Design sponsored by the Department of Business, Energy and Industry Strategies (BEIS) of the UK (Ref 1659/10/2018). We really appreciate the fruitful discussions with the project team members and are especially grateful for the useful feedbacks provided by C. Howlett and R. Underhill of Frazer-Nash Consultancy. The authors would like to thank M. Ferrand and Y. Fournier for technical support for Code_Saturne. The authors would also thank the Collaborative Computational Project (CCP) for nuclear thermal hydraulics (No. EP/T026685/1).

References

Ang, M.L., Aytekin, A., Fox, A.H., 1988. Analysis of flow distribution in a PWR fuel rod bundle model containing a blockage - Part 1. A 61% coplanar blockage. Nucl. Eng. Des. 108, 275–294. https://doi.org/10.1016/0029-5493(88)90218-X

Aumiller, D.L., Tomlinson, E.T., Bauer, R.C., 2001. A Coupled RELAP5-3D/CFD methodology with a proof-of-principle calculation. Nucl. Eng. Des. 205, 83–90. https://doi.org/10.1016/S0029-5493(00)00370-8

Bandini, G., Polidori, M., Gerschenfeld, A., Pialla, D., Li, S., Ma, W.M., Kudinov, P., Jeltsov, M., Kööp, K., Huber, K., Cheng, X., Bruzzese, C., Class, A.G., Prill, D.P., Papukchiev, A., Geffray, C., Macian-Juan, R., Maas, L., 2015. Assessment of systems codes and their coupling with CFD codes in thermal-hydraulic applications to innovative reactors. Nucl. Eng. Des. 281, 22–38. https://doi.org/10.1016/j.nucengdes.2014.11.003

Bavière, R., Tauveron, N., Perdu, F., Garré, E., Li, S., 2014. A first system/CFD coupled simulation of a complete nuclear reactor transient using CATHARE2 and TRIO-U. Preliminary validation on the Phénnix reactor natural circulation test. Nucl. Eng. Des. 277, 124–137. https://doi.org/10.1016/j.nucengdes.2014.05.031

Bertolotto, D., Manera, A., Frey, S., Prasser, H.M., Chawla, R., 2009. Single-phase mixing studies by means of a directly coupled CFD/system-code tool. Ann. Nucl. Energy 36, 310–316. https://doi.org/10.1016/j.anucene.2008.11.027

Bieder, U., Rashkovan, A., 2019. Baffle jetting: CFD analysis of plain jets impinging on fuel rods. Prog. Nucl. Energy 114, 31–45. https://doi.org/10.1016/j.pnucene.2019.02.006

Brockmeyer, L., Carasik, L.B., Merzari, E., Hassan, Y.A., 2016. CFD Investigation of Wire-Wrapped Fuel Rod Bundle Inner Subchannel Behavior and Dependency on Bundle Size, in: Proceedings of the 24th International Conference on Nuclear Engineering - ICONE 24. pp. 1–9. https://doi.org/10.1007/978-3-319-58460-7_45

Bury, T., 2013. Coupling of CFD and lumped parameter codes for thermal-hydraulic simulations of reactor containment. Comput. Assist. Methods Eng. Sci. 20, 195–206.

Clark, C.G., Lyons, D.G., Neu, W.L., 2014. Comparison of single and overset grid techniques for CFD simulations of a surface effect ship, in: Proceedings of the ASME 2014 33rd International Conference on Ocean, Offshore and Arctic Engineering OMAE 2014. San Francisco, pp. 1–7.

Code_Saturne development team, 2019. Salome_CFD highlights. Code_Saturne UK winter meeting 2019. Manchester, 18-20 December.

Creer, J.M., Bates, J.M., Sutey, A.M., 1979. Turbulent flow in a model nuclear fuel rod bundle containing partial flow blockages. Nucl. Eng. Des. 52(1), 15–33.

Fournier, Y., Bonelle, J., Moulinec, C., Shang, Z., Sunderland, A.G., Uribe, J.C., 2011. Optimizing Code_Saturne computations on Petascale systems. Comput. Fluids 45, 103–108. https://doi.org/10.1016/j.compfluid.2011.01.028

Gibeling, H., Mahaffy, J.H., 2002. Benchmarking Simulations with CFD to 1-D Coupling, Joint IAEA/OECD Technical Meeting on Use of CFD Codes for Safety Analysis of Reactor Systems, Including Containment. Pisa, Italy.

Grunloh, T.P., Manera, A., 2017. A novel multi-scale domain overlapping CFD/STH coupling methodology for multi-dimensional flows relevant to nuclear applications. Nucl. Eng. Des. 318, 85–108. https://doi.org/10.1016/j.nucengdes.2017.03.027

Grunloh, T.P., Manera, A., 2016. A novel domain overlapping strategy for the multiscale coupling of CFD with 1D system codes with applications to transient flows. Ann. Nucl. Energy 90, 422–432. https://doi.org/10.1016/j.anucene.2015.12.027

Hanna, B.N., Dinh, N.T., Youngblood, R.W., Bolotnov, I.A., 2020. Machine-learning based error prediction approach for coarse-grid Computational Fluid Dynamics (CG-CFD). Prog. Nucl. Energy 118, 103140. https://doi.org/10.1016/j.pnucene.2019.103140

Jarkowski1, M., M.A. Woodgate, G.N.Barakos, Rokicki, J., 2014. Towards consistent hybrid overset mesh methods for rotorcraft CFD. Int. J. Numer. Methods Fluids 74, 543–576. https://doi.org/10.1002/fld

Kim, W.S., He, S., Jackson, J.D., 2005. Modelling of turbulent heat transfer to fluid at supercritical pressure using adaptive mesh generation, in: Proceedings of TSFP-4. Williamsburg, Virginia, pp. 877–882.

Liu, B., He, S., Moulinec, C., Uribe, J., 2019. Sub-channel CFD for nuclear fuel bundles. Nucl. Eng. Des. 355, 110318. https://doi.org/10.1016/j.nucengdes.2019.110318

Norman, E.S., Stuart, E.R., William, E.D., 2002. PEGASUS 5: An Automated pre-processor for overset-grid CFD, in: 32nd AIAA Fluid Dynamics Conference and Exhibit. Reston, pp. 20191–4344.

Papukchiev, A., Jeltsov, M., Kööp, K., Kudinov, P., Lerchl, G., 2015. Comparison of different coupling CFD-STH approaches for pre-test analysis of a TALL-3D experiment. Nucl. Eng. Des. 290, 135–143. https://doi.org/10.1016/j.nucengdes.2014.11.008

Papukchiev, A., Lerchl, G., Waata, C., Frank, T., 2009. Extension of the simulation capabilities of the 1D system code ATHLET by coupling with the 3D CFD software package ANSYS CFX, in: Proceedings of The 13th International Topical Meeting on Nuclear Reactor Thermal Hydraulics (NURETH-13). Kanazawa City, pp. 1–13.

Papukchiev, A., Lerchl, G., Weis, J., Scheuerer, M., Austregesilo, H., 2011. Development of a coupled 1D-3D Thermal-Hydraulic Code for Nuclear Power Plant Simulation and its Application to a Pressurized Thermal Shock Scenario in PWR, in: Proceedings of 14th International Topical Meeting on Nuclear Reactor Thermalhydraulics Conference (NURETH-14). Toronto.

Pialla, D., Tenchine, D., Li, S., Gauthe, P., Vasile, A., Baviere, R., Tauveron, N., Perdu, F., Maas, L., Cocheme, F., Huber, K., Cheng, X., 2015. Overview of the system alone and system/CFD coupled calculations of the PHENIX Natural Circulation Test within the THINS project. Nucl.

Eng. Des. 290, 78–86. https://doi.org/10.1016/j.nucengdes.2014.12.006

Sitaraman, J., Floros, M., Wissink, A.M., Potsdam, M., 2008. Parallel unsteady overset mesh methodology for a multi-solver paradigm with adaptive cartesian grids. Collect. Tech. Pap. - AIAA Appl. Aerodyn. Conf. https://doi.org/10.2514/6.2008-7177

Tang, H.S., Jones, S.C., Sotiropoulos, F., 2003. An overset-grid method for 3D unsteady incompressible flows. J. Comput. Phys. 191, 567–600. https://doi.org/10.1016/S0021-9991(03)00331-0

Todreas, N.E., Kazimi, M.S., 1990. Nuclear Systems I: Thermal Hydraulic Fundamentals. Taylor & Francis.

Toti, A., Vierendeels, J., Belloni, F., 2017. Improved numerical algorithm and experimental validation of a system thermal-hydraulic/CFD coupling method for multi-scale transient simulations of pool-type reactors. Ann. Nucl. Energy 103, 36–48. https://doi.org/10.1016/j.anucene.2017.01.002

Vassberg, J.C., Buning, P.G., C.L., R., 2002. Drag prediction for the DLR-F4 wing/body using OVERFLOW and CFL3D on an overset mesh, in: 40th AIAA Aerospace Sciences Meeting & Exhibit. Reston, p. 22091.

Viellieber, M., Class, A., 2015. Coarse-Grid-CFD for the Thermal Hydraulic Investigation of Rod-Bundles. Pamm 15, 497–498. https://doi.org/10.1002/pamm.201510239

Völkner, S., Brunswig, J., Rung, T., 2017. Analysis of non-conservative interpolation techniques in overset grid finite-volume methods. Comput. Fluids 148, 39–55. https://doi.org/10.1016/j.compfluid.2017.02.010

Wissink, A.M., Sitaraman, J., Sankaran, V., Mavriplis, D.J., Pulliam, T.H., 2008. A multi-code python-based infrastructure for overset CFD with adaptive cartesian grids. 46th AIAA Aerosp. Sci. Meet. Exhib. 1–18.